HAL
open science

# Thermal evolution of an early magma ocean in interaction with the atmosphere

Thomas Lebrun, Hélène Massol, Eric Chassefière, Anne Davaille, Emmanuel Marcq, Philippe Sarda, François Leblanc, Geneviève Brandeis

## To cite this version:

Thomas Lebrun, Hélène Massol, Eric Chassefière, Anne Davaille, Emmanuel Marcq, et al.. Thermal evolution of an early magma ocean in interaction with the atmosphere. Journal of Geophysical Research. Planets, 2013, 118 (6), pp.1155-1176. 10.1002/jgre.20068 . hal-00799240

**HAL Id: hal-00799240**

**https://hal.science/hal-00799240v1**

Submitted on 23 Apr 2016

**HAL** is a multi-disciplinary open access archive for the deposit and dissemination of scientific research documents, whether they are published or not. The documents may come from teaching and research institutions in France or abroad, or from public or private research centers.

L'archive ouverte pluridisciplinaire **HAL**, est destinée au dépôt et à la diffusion de documents scientifiques de niveau recherche, publiés ou non, émanant des établissements d'enseignement et de recherche français ou étrangers, des laboratoires publics ou privés.

# Thermal evolution of an early magma ocean in interaction with the atmosphere

T. Lebrun,[1] H. Massol,[1] E. Chassefière,[1] A. Davaille,[2] E. Marcq,[3] P. Sarda,[1] F. Leblanc,[3] and G. Brandeis[4]

Received 18 July 2012; revised 13 February 2013; accepted 4 March 2013; published 3 June 2013.

[1] The thermal evolution of magma oceans produced by collision with giant impactors late in accretion is expected to depend on the composition and structure of the atmosphere through the greenhouse effect of $CO_2$ and $H_2O$ released from the magma during its crystallization. In order to constrain the various cooling timescales of the system, we developed a 1-D parameterized convection model of a magma ocean coupled with a 1-D radiative-convective model of the atmosphere. We conducted a parametric study and described the influences of the initial volatile inventories, the initial depth of the magma ocean, and the Sun-planet distance. Our results suggest that a steam atmosphere delays the end of the magma ocean phase by typically 1 Myr. Water vapor condenses to an ocean after 0.1, 1.5, and 10 Myr for, respectively, Mars, Earth, and Venus. This time would be virtually infinite for an Earth-sized planet located at less than 0.66 AU from the Sun. Using a more accurate calculation of opacities, we show that Venus is much closer to this threshold distance than in previous models. So there are conditions such as no water ocean is formed on Venus. Moreover, for Mars and Earth, water ocean formation timescales are shorter than typical time gaps between major impacts. This implies that successive water oceans may have developed during accretion, making easier the loss of their atmospheres by impact erosion. On the other hand, Venus could have remained in the magma ocean stage for most of its accretion.

**Citation:** Lebrun, T., H. Massol, E. Chassefière, A. Davaille, E. Marcq, P. Sarda, F. Leblanc, and G. Brandeis (2013), Thermal evolution of an early magma ocean in interaction with the atmosphere, *J. Geophys. Res. Planets*, *118*, 1155–1176, doi:10.1002/jgre.20068.

## 1. Introduction

[2] It is now established that during accretion, most of the terrestrial planets underwent a magma ocean stage [*Wood et al.*, 1970; *Hostetler and Drake*, 1980; *Samuel*, 2012; for a general review, see also *Elkins-Tanton*, 2012]. The total or partial melting of a planetary mantle is due to a combination of heat sources such as the energy provided by impacts, radioactive decay, heat losses from the core at the CMB, and tidal heating if there is another planet nearby (like the Moon in the case of the Earth). Although not yet clearly established, it is likely that at the end of accretion, giant impacts could have melted the entire mantle of the planet [*Tonks and Melosh*, 1993; *Reese and Solomatov*, 2006]. The subsequent cooling history of this magma ocean will set the initial conditions for the appearance and style of tectonic regimes prevailing in the solid-state mantle and for the planet habitability at early ages. The presence and nature of an atmosphere will greatly influence the evolution of the system since the greenhouse effect of a steam atmosphere resulting from the outgassing of the magma ocean is expected to slow down the radiation of heat to space, and therefore to decrease the cooling rate of the system.

[3] In recent years, several models investigated the thermal evolution of a magma ocean. Early models [*Abe and Matsui*, 1985] consider Earth growing by planetesimal impacts, then cooled conductively through a grey radiative atmosphere. Later additions to this model consist in a more realistic water repartition between atmosphere and magma [*Abe and Matsui*, 1986]. Following these two papers, a radiative-convective atmosphere is then taken into account, thus slowing down the cooling of the magma ocean [*Abe and Matsui*, 1988; *Zahnle et al.*, 1988]. These models set the basis for future studies of thermal evolution of the magma ocean and the overlying atmosphere. *Abe* [1997] took into account variable viscosity with crystal content, phase changes during cooling, and an overlying steam atmosphere, however not explicitly coupled with the degassing magma ocean. Following these studies, *Elkins-Tanton* [2008] explicitly coupled the degassing of volatiles through a grey radiative atmosphere, however

[1]IDES/UMR 8148/CNRS/Université Paris-Sud, Orsay, France.
[2]FAST/UMR 7608/CNRS/Université Paris-Sud, Orsay, France.
[3]LATMOS/UMR 8190/CNRS/Université de Versailles St-Quentin-en-Yvelines, Versailles, France.
[4]LDFG/Institut de Physique du Globe de Paris/Sorbonne Paris Cité/Univ. Paris Diderot/UMR 7154/CNRS, Paris, France.

Corresponding author: T. Lebrun, Laboratoire IDES, Univ. Paris Sud, Batiment 509, Rue du Belvédère, Campus Universitaire d'Orsay, 91405 Orsay, France. (thomas.lebrun@u-psud.fr)

©2013. American Geophysical Union. All Rights Reserved.
2169-9097/13/10.1002/jgre.20068

considering a constant viscosity varying between 0.1 and 1 Pa s. This latter work that takes into account the chemical evolution of the crystallizing phases, predicts a gravitational overturn once solidification is completed due to the unstable density stratification resulting from the cooling of the magma ocean. Another major energy source to be considered, albeit only relevant to the young Earth, is the tidal heating caused by the much nearer Moon. *Zahnle et al.* [2007] showed that the resultant heating could overwhelm the radioactive heating, thus expanding the lifetime of a magma ocean. These models lead to very different estimates of cooling time scales varying from 400 years [*Solomatov*, 2000]) to 100 million years [*Abe*, 1997]. As shown by this brief review, the models have progressively taken into account more and more of the complexities of magma ocean dynamics. In comparison, the models taken for the atmosphere were much simpler. However, it has been recently shown from a one-dimensional radiative-convective model of a massive $H_2O$-$CO_2$ atmosphere [*Marcq*, 2012] that a more realistic treatment of the atmospheric dynamics could have an important effect. The opacities in the thermal infrared (IR) have been computed using a *k*-correlated code, tabulated continuum opacities for $H_2O$-$H_2O$ and $CO_2$-$CO_2$ absorption and water clouds in the moist convective zone (whenever present). Two regimes have been identified. For a surface temperature smaller than a threshold temperature (of 2350 K for 300 bars of $H_2O$ and 100 bars of $CO_2$), an efficient greenhouse effect results in a cool upper atmosphere and a water cloud cover, slowing down the radiation of the heat released by the magma ocean to space. For a surface temperature larger than the threshold, the greenhouse effect is not efficient enough to prevent large radiative heat loss to space through a hot, cloudless atmosphere. The transition from large to small radiative heat loss to space, when the surface temperature drops below the threshold temperature, could play a major role in slowing down the cooling of the magma ocean.

[4] It is also essential to determine the conditions under which water could condensate into an ocean at the surface of the planet. One of the important objectives of the present work is to better understand the conditions and timing of the formation of the terrestrial ocean of water, and why such an ocean did not form on Venus, or possibly formed at an early stage but later evaporated due to the increasing luminosity of the young Sun. The presence of an early massive atmosphere of water vapor on Venus, which further escaped to space and/or was trapped in the interior under the form of hydrates, is generally considered to have initiated the strong greenhouse effect observed today [*Shimazu and Urabe*, 1968; *Rasool and de Bergh*, 1970]. This massive $H_2O$ atmosphere may have resulted either (i) from the evaporation of a primordial water ocean, followed by the hydrodynamic escape of hydrogen [*Kasting*, 1988], or (ii) from the outgassing of the primordial magma ocean, not necessarily followed by the formation of a (transient) water ocean [*Gillmann et al.*, 2009]. Determining through a comparative modeling approach applied to the three terrestrial planets Mars, Earth, and Venus if a water ocean ever condensed on Venus and, if so, how long this ocean survived is one of the major challenges of modern exobiology.

[5] So in the present model we solve simultaneously (i) the thermal evolution of the convective magma ocean (based on Solomatov parametric scaling [*Solomatov*, 2000, 2007]) and the radiative-convective atmosphere and (ii) the volatile exchange between the magma ocean and the atmosphere. In the latter, the effects of (1) the convection in the troposphere, (2) the presence of water clouds, (3) the condensation of water vapor, and (4) the pressure contribution of $N_2$ gas are included. At each time, the atmosphere should be in volatile equilibrium with the magma ocean. The dynamics of the magma ocean have been simplified compared to some previous models. We do not take into account the effect of tidal heating [*Zahnle et al.*, 2007] on the magma ocean cooling, nor the effect of the rotation on the convective patterns. We also do not resolve in details the sequence of petrological phases which crystallize as the magma ocean cools down [*Elkins-Tanton*, 2008], but we include the influence of the depth dependence of the solidus-liquidus curves on the magma ocean solidification. Moreover, we take into account the variations of the magma viscosity with temperature and crystal content in the convective modeling. We shall see that these viscosity variations are not negligible regarding the cooling time scale. Our simple parametric approach, which is focused on the estimate of cooling timescales (formation of the water ocean and early tectonic plates), is therefore complementary of more complex petrological models using 2-D or 3-D convection codes [*Breuer and Moore*, 2007].

[6] Section 2 describes our model and assumptions. In section 3, we first study the influence of a dense steam atmosphere on the thermal evolution of the system, and the main differences when compared to the cases for which (i) no atmosphere is present and (ii) the atmosphere is treated as a grey emitter [*Elkins-Tanton*, 2008]. Then we investigate the influence of (1) volatile inventory and degassing path, (2) radiogenic heat production rate, and (3) distance from the Sun. We finally discuss in section 4 the implications of our results on the conditions and timing of the formation of a water ocean for Venus, Earth, and Mars.

## 2. The Model

[7] We model the secular cooling of the magma ocean by convective transport of heat in a 1-D spherically symmetric geometry. The magma ocean model is coupled to a radiative-convective thermal model of the atmosphere [*Marcq*, 2012] through the exchange of volatile species between the magma ocean and the atmosphere and the conservation of heat at the interface between the magma ocean and the atmosphere. In the following sections, we detail the model setup and equations. A flowchart designed to explicitly show how the main variables are implemented is given in section A.

### 2.1. Initial State

[8] In the initial state, we consider a potential temperature $T_{p_i}$ of 4000 K. Given the Earth's mantle liquidus (Figure 1), this temperature would correspond to the Earth's mantle being molten all the way to the core-mantle boundary.

[9] To determine the initial surface temperature $T_{s_i}$, we consider that the heat flux at the surface of the planet $F$ is in equilibrium with the blackbody flux $F_b = \sigma(T_s^4 - T_{eq}^4)$ where $T_{eq}$ is the equilibrium temperature of the planet. That amounts to consider that the planet initially has no atmosphere.

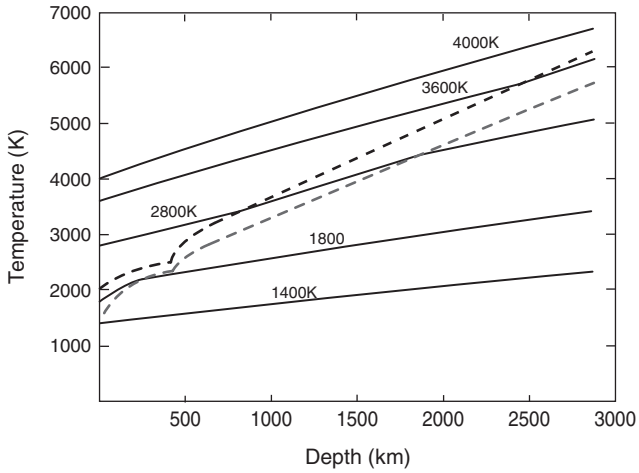


**Figure 1.** Liquidus (black dashed line), solidus (grey dashed line) redrawn after *Abe* [1997]. Adiabatic temperature profiles (black lines) correspond to a magma ocean with the thickness of the Earth's mantle. As cooling proceeds, adiabats cross the liquidus then solidus curves, the magma ocean solidifying from below [see also *Elkins-Tanton*, 2008; *Solomatov*, 2000].

[10] Initial amounts of volatiles vary from $1.4 \times 10^{-2}$ to $1.4 \times 10^{-1}$ wt % for $CO_2$ and $H_2O$ corresponding to partial pressures varying between 100 and 1000 bars.

### 2.2. Convective Cooling of the Magma Ocean

[11] After an impact, the magma ocean is losing its heat due to cooling through its upper surface with the atmosphere. The convection is characterized by two dimensionless parameters, the Prandtl number $Pr = \nu/\kappa$ which compares the viscous to the thermal dissipation, and the Rayleigh number which compares the buoyancy force to the thermal and viscous dissipations:

$$Ra = \frac{\alpha g \left(T_p - T_s\right) l^3}{\kappa \nu} \tag{1}$$

where $T_s$ is the surface temperature, $\kappa$ is the thermal diffusivity, $k = \kappa \rho C_p$ is the thermal conductivity, $l$ is the length scale corresponding in our case to the magma ocean thickness, $\nu = \eta/\rho$ is the kinematic viscosity, and $\eta$ is the dynamic viscosity at the temperature $T_p$ of the magma ocean interior. For the magma ocean, $Pr \sim 100$, while for a solid mantle, $Pr$ is quasi-infinite ($\sim 10^{23}$). Due to the large thickness of the magma ocean (2900 km if it englobes the whole mantle) and the low viscosity of the magma at high temperature (typically 0.1 Pa.s) [i.e., *Solomatov*, 2000], $Ra$ is high even for a very small temperature difference between the surface and the interior of the magma ocean (i.e., $Ra \sim 10^{26}$ for $\Delta T = T_p - T_s = 1$ K). Therefore the magma ocean is expected to convect vigorously and its interior should be well mixed. In this case we can assume that its internal temperature, $T(r, t)$, follows an adiabatic profile. The magma ocean temperature evolution is governed by the conservation of energy [e.g., *Abe*, 1997]:

$$r^2 \rho \left( C_p + \Delta H \frac{\mathrm{d}\phi}{\mathrm{d}T} \right) \frac{\mathrm{d}T}{\mathrm{d}t} = \frac{\partial}{\partial r} \left( r^2 F_r \right) + r^2 \rho q_r, \tag{2}$$

where $r$ is the planetocentric altitude, that is, the distance from the center of the planet, $T$ is the temperature, $C_p$ is the specific heat, $\Delta H$ is the difference of specific enthalpy between melt and solid phases, $F_r$ is the convective heat flux at radius r, $q_r$ is the radiogenic heat production rate, and $\rho$ is the average magma density defined as $\rho = \rho_s \rho_m / (\rho_m (1 - \phi) + \rho_s \phi)$ [*Abe*, 1993] , $\rho_m$ being the density of the liquid phase, $\rho_s$ the density of the solid phase, and $\phi$ the melt fraction defined as [*Abe*, 1997]

$$\phi = \frac{T - T_{\mathrm{sol}}}{T_{\mathrm{liq}} - T_{\mathrm{sol}}}, \tag{3}$$

with $T_{\mathrm{sol}}$ and $T_{\mathrm{liq}}$ being, respectively, solidus and liquidus temperatures. Density variations are only taken into account in buoyancy forces (Boussinesq approximation). Temperatures $T_{\mathrm{sol}}$ and $T_{\mathrm{liq}}$ are plotted in Figure 1 and are obtained from interpolations of experimentally determined solidus and liquidus temperatures of lherzolite for $P < 23$ GPa and an ideal mixture of $MgSiO_3$-perovskite and MgO at higher pressure after *Takahashi et al.* [1993] and *Zerr and Boehler* [1993, 1994] (for details, see *Abe* [1997]). The term $\Delta H \mathrm{d}\phi/\mathrm{d}T$ represents the latent heat of solidification.

[12] Given the slopes of the liquidus and solidus compared to the adiabats (Figure 1), the cooling magma ocean will solidify starting from the bottom to the surface, as the adiabats cross the liquidus and the solidus curves first in the bottom of the mantle. When the melt fraction increases above a critical melt fraction noted $\phi_c$ ($\phi_c$=0.4), there is an abrupt change in the rheological behavior of the partially crystallized melt [*Arzi*, 1978; *Abe*, 1995]. This drastic change is due essentially to a change in the connectivity of solid particles. We define two main zones, one zone with $\phi > \phi_c$ where the viscosity is that of a magmatic liquid and another zone with $\phi < \phi_c$ where the melt has a solid-like behavior and the viscosity increases drastically. The limit between these two zones is called the rheology front (after *Solomatov* [2000]). As previously mentioned, we suppose an initially completely molten magma ocean of fixed depth $R_p - R_b$, where $R_p$ is the radius of the planet and $R_b$ the planetocentric altitude of the bottom of the magma ocean. As cooling proceeds, radii $R_s$, $R_f$, and $R_l$ (respectively, planetocentric altitudes of the bottom of the solidification front, rheological front, and bottom of the totally liquid zone) move toward the surface (see Figure 2). We suppose that these two layers do not mix based on what takes place in magma chambers [*Turner and Campbell*, 1986; *Jaupart and Brandeis*, 1986]. Indeed, *Turner and Campbell* [1986] showed that for a sufficiently high viscosity difference between two magmas (viscosity ratio of order of 400), the two fluids remain unmixed. In the case of the magma ocean, the viscosity contrast is much higher, on the order of $10^{15}$. Even at the larger convection velocities involved in the magma ocean, it should remain unmixed following Turner and Campbell's criterion. In the partially liquid zone (between $R_f$ and $R_l$ in Figure 2), we assume equilibrium crystallization, which is a good enough approximation for crystals less than 1 mm radius [*Solomatov*, 2007; *Suckale et al.*, 2012]. Because the surface heat flux should not depend too much on the details of solid convection and overturn phenomenon in the solid layer at the base of the magma ocean

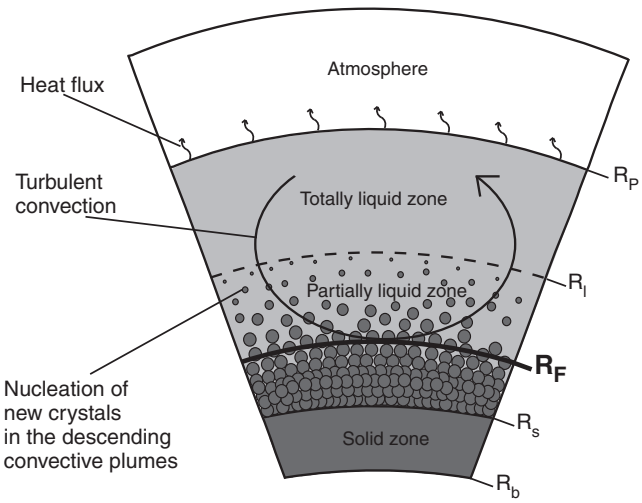


**Figure 2.** Schematic section of the magma ocean adapted from *Solomatov* [2007]. Three zones are pictured: a totally liquid zone when $T > T_{\mathrm{liq}}$. A partially liquid zone when $T_{\mathrm{sol}} < T < T_{\mathrm{liq}}$, and finally a solid zone when $T < T_{\mathrm{sol}}$. We define $R_p$ the radius of the planet, $R_f$ the planetocentric altitude of the bottom of the rheological front, $R_l$ the bottom of the totally liquid zone, $R_s$ the top of the solid zone, and $R_b$ the bottom of the initially molten magma ocean. As cooling proceeds, $R_s$, $R_f$, and $R_l$ move toward the surface.

[*Solomatov*, 2007; *Jaupart and Mareschal*, 2011], we will not consider here the details of petrological nor geochemical processes occurring within this solid layer, even if these processes are essential to understand the present stratification of the Earth [*Elkins-Tanton*, 2008]. The adiabatic temperature profile in each zone is given in section B and can be expressed in terms of the potential temperature. Recent experimental petrological data at high pressure and temperature [*Fiquet et al.*, 2010; *Labrosse et al.*, 2007; *Nomura et al.*, 2011] show that the liquidus and solidus profiles in the very deep mantle could be different from those shown in Figure 1 and allow for the long-term existence of a partially molten zone there. But this is still debated [*Andrault et al.*, 2011]. So in the present work, we will only consider the interaction with the atmosphere of a magma ocean solidifying from its bottom up.

[13] Integrating equation (2) over the whole magma ocean, we obtain (see section B for the full development):

$$I\frac{\mathrm{d}T_p}{\mathrm{d}t} = \left[R_p^2 F\right] + Q_r, \tag{4}$$

where $T_p$ is the potential temperature, that is, the temperature of a parcel of magma ocean decompressed adiabatically to the atmosphere pressure, $Q_r$ is the radiogenic heat production, and $F$ is the heat flux at the magma ocean surface. Equation (4) assumes that the heat flux coming from the core at the bottom of the magma ocean is negligible. $I$ and $Q_r$ are defined in section B.

[14] In Rayleigh-Benard convection, the surface heat flux scales as

$$F = C_0 \frac{k\left(T_p - T_s\right)}{l} Ra^n, \tag{5}$$

where $C_0$ and $n$ are constants which depends on the regime and pattern of convection [*Malkus*, 1954; *Siggia*, 1994; *Grossmann and Lohse*, 2000; *Solomatov*, 2007; *Davaille and Limare*, 2007] and the thermal boundary layer thickness scales as

$$\delta = \frac{k\left(T_p - T_s\right)}{F} \tag{6}$$

[15] An exponent $n = 1/3$ in equation (5) means that heat loss is governed solely by local instabilities of the upper thermal boundary layer (TBL) and does not depend explicitly on the magma ocean thickness. It has been observed in experiments with constant viscosity for $10^6 < Ra < 10^{10}$ with constant $C_0$ varying between 0.05 and 0.18 (see *Siggia* [1994] and *Davaille and Limare* [2007] for a review). On the other hand, the appearance of a large-scale circulation connecting the top TBL to the bottom of the layer, either due to turbulent motions in confined boxes (for $10^8 < Ra < 10^{14}$, see *Castaing et al.* [1989] and *Grossmann and Lohse* [2000]) or due to large viscosity variations [e.g., *Solomatov and Moresi*, 1997; *Androvandi et al.*, 2011] would give an exponent lower than 1/3. For very high $Ra$ (greater than $10^{14}$), it has been proposed that an ultimate regime [*Kraichman*, 1962] could occur where the TBLs are not limiting the heat transport anymore and the exponent is $n = 1/2$. This may have been recently observed in very tall and thin cavities [*Chavanne et al.*, 1997; *Ahlers et al.*, 2012] but the scaling remains controversial and the corresponding flow organization unknown. Anyway, another complication arises for the magma ocean: In its liquid state, its convective pattern and heat transport will be sensitive to rotation. But there again there is no consensus yet on the exponent $n$ which may be much higher than 1/3 [e.g., *King et al.*, 2012]. So it follows that although the regime is not clear for the very high $Ra$ of the magma ocean, a value of $n = 1/3$ is probably a lower conservative bet. That is the value that we shall adopt for the liquid stage of the magma ocean, with $C_0 = 0.089$ [e.g., *Siggia*, 1994].

[16] On the other hand, the definition of $Ra$ (equation (1)) shows that $F$ depends on the viscosity of the magma ocean interior and therefore depends on its temperature and crystal content. It is the strong increase of the viscosity as the magma ocean cools which is going to influence the pattern of convection and therefore the heat flux when the rheological front reaches the surface. We consider that for $\phi > \phi_c$, the viscosity of the magma corresponds to the viscosity of a magmatic liquid containing crystals [*Roscoe*, 1952]:

$$\eta = \frac{\eta_l}{\left(1 - \frac{(1-\phi)}{(1-\phi_c)}\right)^{2.5}}, \tag{7}$$

where [*Karki and Stixrude*, 2010]

$$\eta_l = A \exp\left(\frac{B}{T_p - 1000}\right), \tag{8}$$

is the viscosity of the magmatic liquid derived from the Vogel-Fulcher-Tammann equation where $A = 0.00024$ Pa s and $B = 4600$ K.

[17] For $\phi < \phi_c$ the viscosity of the magma is controlled by the viscosity of the solid particles [*Solomatov*, 2007]:

$$\eta = \eta_s \exp\left(\alpha_n \phi\right), \tag{9}$$

**Table 1.** Constant Physical Parameters

| Symbol | Value | Meaning |
|---|---|---|
| $C_p$ | 1000 J/kg K | Specific heat |
| $\rho_m$ | 4000 kg/m$^2$ | Melt density |
| $\rho_s$ | 4200 kg/m$^2$ | Solid density |
| $\Delta\rho$ | 200 kg/m$^2$ | Solid/melt density difference |
| $\Delta H$ | $4 \times 10^5$ J/kg | Difference of specific enthalpy |
| $\kappa$ | $10^{-6}$ m$^2$/s | Thermal diffusivity |
| $\mu$ | 80 GPa | Shear modulus |
| $A$ | $5.3 \times 10^{15}$ | Pre-exponential factor |
| $h$ | 1 mm | Grain size |
| $b$ | 0.5 nm | Burger vector length |
| $E$ | 240 kJ/mol | Activation energy |
| $V$ | 5 cm$^3$/mol | Activation volume |
| $R$ | 8.314 J/mol K | Gas constant |
| $\alpha_n$ | 26 | Coefficient in melt fraction-dependent viscosity |
| $t_0$ | 4.55 Gyr | Age of the Earth |

with [*Karato and Wu*, 1993]

$$\eta_s = \frac{\mu}{2A}\left(\frac{h}{b}\right)^{2.5} \exp\left(\frac{E+PV}{RT_p}\right), \tag{10}$$

where $\eta_s$ is the solid dynamic viscosity, $\mu$ is the shear modulus, $A$ is the pre-exponential factor, $h$ is the grain size, $b$ is the Burger vector length, $E$ is the activation energy, $V$ is the activation volume, $R$ is the perfect gas constant, and $\alpha_n$ is a constant which depends on the creep mechanism. For low stress, low temperatures and high pressure, the diffusion creep mechanism is favored compared to dislocation creep [*Karato and Wu*, 1993]. For wet diffusion creep, $\alpha_n$=26 [*Mei et al.*, 2002]. Unlike previous models, we therefore include the explicit dependence of the viscosity of magma on the potential temperature, in addition to its dependence on the fraction of crystals.

[18] When, due to cooling, the rheology front ($\phi < 0.4$) reaches the surface of the planet, the type of convection changes. The drastic increase in viscosity at the surface marks the beginning of the growth of a thicker cold viscous thermal boundary layer and also changes the convective regime. Numerical simulations [e.g., *Solomatov and Moresi*, 1997] and laboratory experiments [e.g., *Androvandi et al.*, 2011] showed that for very large variations of viscosity, convection involving the subduction of highly viscous lids is such that $n = 0.29$. Moreover, including the resistance of lithospheric TBL to bending at subduction zones [*Conrad and Hager*, 1999] and/or the effects of a basaltic crust [*Davies*, 1999] or of dehydration on TBL viscosity and density [*Korenaga*, 2006] further lowers the exponent $n$. To take into account this regime of convection, we decrease in our model the exponent $n$ to a value of 0.25. This regime is certainly closer to plate tectonics than the turbulent liquid magma ocean, and it is tempting to assimilate the cold viscous top TBL with a "lithospheric plate." However, the transition from a liquid magma ocean to plate tectonics in a solid-state mantle is still debated and probably very complicated [see *Bercovici et al.*, 2000; *Van Hunen et al.*, 2008; *Lowman*, 2011]. Our very simplified model is just a first approximation.

[19] Within the framework detailed above, the cooling of the magma ocean thus occurs in three main stages: (i) a first stage, when the magma ocean is completely molten, (ii) a second stage where crystals are mixed with melt and the rheology front moves upward to the surface, and finally (iii) a third stage, which is called "Mush" stage in the next section and which begins when the rheology front ($\phi < 0.4$) reaches the surface. It also dates the end of the magma ocean phase.

[20] The radiogenic heat production rate $q_r$ is determined from the current concentrations of uranium, thorium and, potassium [*Schubert et al.*, 2001; *Jaupart and Mareschal*, 2011]. We also introduce the radiogenic heat production rate from the initial concentration of $^{26}$Al because this radioactive isotope may have a significant influence on the beginning of the solidification of the magma ocean. From the initial concentration and the law of radioactive decay, we determine the time evolution of each radioactive isotope. The radiogenic heat production rate is then written as follows:

$$\begin{aligned} q_r = {} & 0.9928[\mathrm{U}]_a H_{^{238}\mathrm{U}} \exp\left(-\lambda_{^{238}\mathrm{U}}(t-t_0)\right) \\ & + 0.0072[\mathrm{U}]_a H_{^{235}\mathrm{U}} \exp\left(-\lambda_{^{235}\mathrm{U}}(t-t_0)\right) \\ & + [\mathrm{Th}]_a H_{^{232}\mathrm{Th}} \exp\left(-\lambda_{^{232}\mathrm{Th}}(t-t_0)\right) \\ & + 1.17 \times 10^{-4}[\mathrm{K}]_a H_{^{40}\mathrm{K}} \exp\left(-\lambda_{^{40}\mathrm{K}}(t-t_0)\right) \\ & + 5 \times 10^{-5}[\mathrm{Al}]_a H_{^{26}\mathrm{Al}} \exp\left(-\lambda_{^{26}\mathrm{Al}} t\right) \end{aligned} \tag{11}$$

where $\lambda_i$ are the decay constants for each isotope, $H$ is the heat production per unit mass of isotope, and $t_0$ is the age of the planet (see Table 1). Element concentrations $[\mathrm{U}]_a$, $[\mathrm{Th}]_a$, $[\mathrm{K}]_a$, and $[\mathrm{Al}]_a$ are present-day values appropriate to the silicate Earth, for which we use typical chondritic values (see Table 2) [*Allègre et al.*, 1995; *McDonougha and Sun*, 1995; *Taylor and McLennan*, 1995; *Lodders and Fegley*, 1998; *Javoy*, 1999].

### 2.3. The Atmosphere-Magma Ocean Coupling

[21] The thermal model described above is designed to be coupled with a radiative-convective atmospheric model [*Marcq*, 2012]. The upward radiative atmospheric heat flux at the surface must balance the convective heat flux out of the mantle. In order to calculate the atmospheric heat flux it is necessary to determine the surface temperature. The detailed structure of the boundary layer is not calculated explicitly but the surface temperature can be derived iteratively from equation (5) and section A shows how the model is implemented. As the magma ocean cools, volatiles are exsolved to the atmosphere. The convective velocity of the magma for liquid-state convection is

**Table 2.** Heat Production Parameters[a]

| Isotope/Element | Half-Time (year) | Heat Production Per Unit Mass Of Isotope (W/kg) | Natural Abundance (%) | Current Concentrations (ppm) |
|---|---|---|---|---|
| $^{238}$U | $4.46 \times 10^9$ | $9.17 \times 10^{-5}$ | 99.28[b] | |
| $^{235}$U | $7.04 \times 10^8$ | $5.75 \times 10^{-4}$ | 0.72[b] | |
| U | | | | 0.20 [*Javoy*, 1999] |
| $^{232}$Th | $1.40 \times 10^{10}$ | $2.56 \times 10^{-5}$ | 100[b] | |
| Th | | | | 0.069 [*Javoy*, 1999] |
| $^{40}$K | $1.26 \times 10^9$ | $2.97 \times 10^{-5}$ | 0.0117[b] | |
| K | | | | 270 [*Javoy*, 1999] |
| $^{26}$Al | $7.17 \times 10^5$ | $3.54 \times 10^{-1}$ | 0.005[c] | |
| Al | | | | 8650 [*Lodders and Fegley*, 1998] |

[a]From *Rybach* [1988] for U, Th, and K and *Sramek et al.* [2011] for Al.
[b]Current natural abundance.
[c]Initial natural abundance.

given as follows [*Priestley*, 1957, 1959; *Solomatov*, 2007; *Elkins-Tanton*, 2008]:

$$v_{\text{conv}} = 0.6\left[\frac{\alpha g l F}{\rho C_p}\right]^{1/3} \tag{12}$$

[22] The convection velocity is on the order of 0.15–5 m s$^{-1}$ at the beginning of the magma ocean solidification. When the rheology front reaches the surface, we switch to another type of convection which is close to solid-state convection. Considering a magma ocean with a depth equal to the thickness of the present Earth's mantle, convection runs to completion in 1 week up to a few months when it is vigorous, and up to a maximum of several millions years when it is closed to solid-state convection. Compared to the magma ocean cooling time, we assume that for liquid-state convection, the mass fraction of dissolved volatile in the magma ocean is in equilibrium with the atmospheric volatile content at each time step due to convective currents at different scales. When we approach solid-state convection, we consider that volatiles are carried up and then exsolved by melt percolation through channels through a porous media. The percolation velocity is given as follows [*Solomatov*, 2007]:

$$v_{\text{perc}} = \frac{g\Delta\rho d^2 \phi_l^2}{150\eta_l(1-\phi_l)} \tag{13}$$

[23] The percolation velocity being higher than the velocity of the solidification front, we assume that volatiles can travel up to the surface more rapidly than the solidification front propagates, and we consider that the mass fraction of dissolved volatiles in the liquid part of the magma ocean is in equilibrium with atmospheric volatile content at each time step.

[24] The volatile mass balance is given as follows:

$$k_{\text{vol}} X_{\text{vol}} M_{\text{solid}} + X_{\text{vol}} M_{\text{liquid}} + \frac{4\pi R_p^2}{g} P(X_{\text{vol}}) = X_0 M_0 \tag{14}$$

where $k_{\text{vol}}$ is the distribution coefficient for each volatile species between the solid and liquid phases,

$$k_{\text{vol}} = \frac{M_{s_{\text{perov}}} k_{\text{vol}_{\text{perov}}} + M_{s_{\text{lherz}}} k_{\text{vol}_{\text{lherz}}}}{M_{s_{\text{perov}}} + M_{s_{\text{lherz}}}} \tag{15}$$

where $M_{s_{\text{perov}}}$ and $M_{s_{\text{lherz}}}$ are, respectively, the masses of the solid phases for perovskite and lherzolite, $k_{\text{vol}_{\text{perov}}}$ the partition coefficient of volatile ($H_2O$ or $CO_2$) for perovskite, and $k_{\text{vol}_{\text{lherz}}}$ the partition coefficient for lherzolite (see Table 3) [*Elkins-Tanton*, 2008]. Variable $X_{\text{vol}}$ is the mass fraction of volatiles in the magma, $M_{\text{liquid}}$ is the mass of liquid phase, $M_{\text{solid}}$ is the mass of solid phase, $X_0$ is the initial mass fraction of volatiles, $M_0$ is the initial mass of liquid and $P(X_{\text{vol}})$ is the partial pressure of volatiles in the gas phase [*Caroll and J. R. Holloway (Eds.)* 1994]:

$$P(X_{H_2O}) = \left(\frac{X_{H_2O}}{6.8 \times 10^{-8}}\right)^{1/0.7}, \tag{16}$$

[*Pan et al.*, 1991]

$$P(X_{CO_2}) = \frac{X_{CO_2}}{4.4 \times 10^{-12}}. \tag{17}$$

[25] Partial pressures are then used as inputs for the atmospheric model. Indeed, the greenhouse effect depends on the opacity of the atmosphere which varies with the relative proportion of each gaseous component.

## 3. Results

### 3.1. Influence of a Primitive Massive Atmosphere

[26] The atmospheric model used in the simulation is described in details in a previous paper by *Marcq* [2012]. It takes into account two major greenhouse gases: $H_2O$ and $CO_2$. We have used in the nominal case a content of $H_2O$ similar to the content of Earth's ocean, equivalent to a partial pressure of 300 bars $H_2O$ ($4.3 \times 10^{-2}$ wt %) by assuming that all the oceanic water is present as vapor in the atmosphere. For Venus and Mars, we have scaled this value by assuming that the ratio of the mass of water to the mass of the planet is the same, as expected if the three planets were formed from embryos with the same water content. We have proceeded in the same way for $CO_2$, by choosing a pressure of 100 bars ($1.4 \times 10^{-2}$ wt %), that is, a $CO_2$ content equivalent to its Venus atmospheric content.

[27] It is generally thought that the present Earth's mantle could contain the equivalent of one ocean; thus, the

**Table 3.** Value of Distribution Coefficients for $H_2O$ and $CO_2$ Used in This Study

| Symbol | Value |
|---|---|
| $k_{H_2O_{\text{perov}}}$ | $10^{-4}$ |
| $k_{CO_{2_{\text{perov}}}}$ | $5 \times 10^{-4}$ |
| $k_{H_2O_{\text{lherz}}}$ | $1.1 \times 10^{-2}$ |
| $k_{CO_{2_{\text{lherz}}}}$ | $2.1 \times 10^{-3}$ |

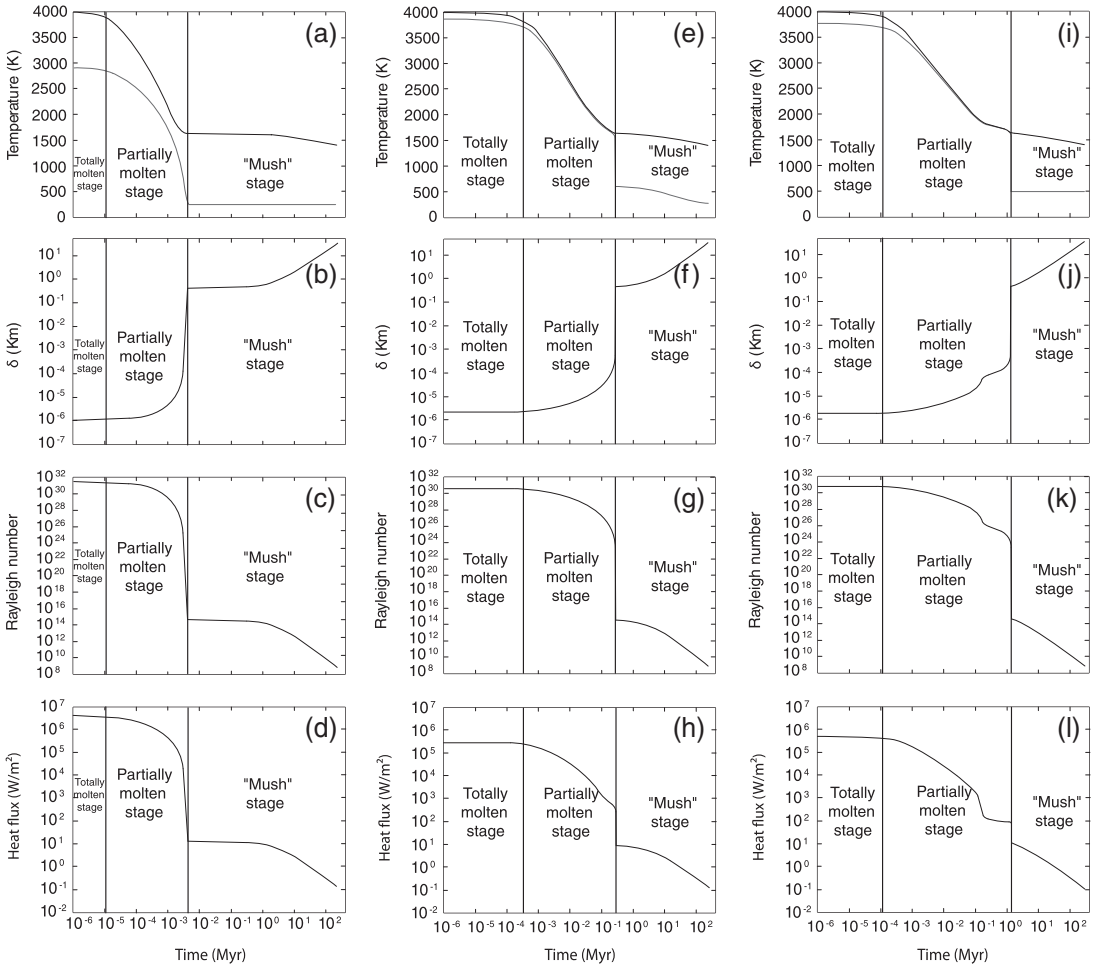


**Figure 3.** Time evolution of main parameters when (1) (a–d) no atmosphere is present, (2) (e–h) the atmosphere is treated as a grey emitter [*Elkins-Tanton*, 2008], and (3) (i–l) coupling with our convective-radiative atmospheric model. Time evolution of surface (grey line) and potential (black line) temperatures (Figures 3a, 3e, and 3i), boundary layer thickness (Figures 3b, 3f, and 3j), Rayleigh number (Figures 3c, 3g, and 3k), and heat flux (Figures 3d, 3e, and 3h). For the three above cases, the beginning of the mush stage corresponds to the time at which a cold boundary layer ($t_p$) starts to grow. Condensation of vapor water also occurs at that time ($t_c$). The end of "Hard magma ocean"stage [*Abe*, 1993] defined when the heat flux drops below 1 W m$^{-2}$ corresponds here to 30 Myr. Parameters used for the calculations are given in Table 4.

total inventory of Earth could be two oceans, or even more if the mantle is richer in water than estimated. The initial inventory of $H_2O$ on terrestrial planets may have been much larger [*Raymond et al.*, 2006], up to several tens of oceans, but hydrodynamic escape could have removed most of the initial water [see, e.g., *Gillmann et al.*, 2009]. In the present study, we will consider initial $H_2O$ and $CO_2$ inventories up to an equivalent partial pressure of 1000 bars. We also take into account a constant $N_2$ partial pressure of 5 bars throughout the solidification of the magma ocean. A comparison between a magma ocean without overlying atmosphere and a magma ocean coupled with a massive atmosphere is shown in Figure 3.

[28] The viscosity of the magma ocean increases drastically when the rheology front ($\phi < 0.4$) reaches the surface as illustrated by the decrease of the Rayleigh number (Figures 3c, 3g, and 3k) indicating a weakening of the convection associated with the increase of the thickness of the surface boundary layer up to about 1 km at that stage (Figures 3b, 3f, and 3j).

[29] The growth of the boundary layer corresponds to a drop in surface temperature due to the viscosity increase at that time. This cold solid-like boundary layer is very thin when it first forms. It should break easily at the surface of the magma ocean. The type of convection changes at that time, switching to solid-like convection (hard ocean regime of *Abe* [1997]). At this stage, the solid volume fraction reaches ≈98% (vertical dashed lines in figures). To give an order of magnitude, if we assume that all the magmatic liquid corresponding to this percentage is located at the surface of the mantle, the thickness of liquid is equal to about 35 km, which roughly corresponds to the thickness of the oceanic lithosphere. At present time, the total melt fraction of the mantle is estimated to be smaller than 0.1% [*Hirschmann*, 2009]. At further stages, beyond 98% of solid volume fraction, heat transfer is ensured by solid convection, which

**Table 4.** Physical Parameters Used in This Study

| Figures | $X_{0_{H_2O}}$ ($10^{-2}$ wt %) | $X_{0_{CO_2}}$ ($10^{-2}$ wt %) | Distance from the Sun (au) | Gravitational Acceleration $g$ (m s$^{-2}$) | Planetary Radius $R_p$ (km) | Initial Depth ($R_p - R_b$) (km) |
|---|---|---|---|---|---|---|
| Figures 3a–3d | / | / | 1 | 9.8 | 6378 | 2885 |
| Figures 3e–3l | 4.3 | 1.4 | 1 | 9.8 | 6378 | 2885 |
| Figure 4 | 1.4–14.3 | 1.4–14.3 | 1 | 9.8 | 6378 | 2885 |
| Figure 5a | 1.4 | 1.4 | 1 | 9.8 | 6378 | 2885 |
| Figure 5b | 14.3 | 1.4 | 1 | 9.8 | 6378 | 2885 |
| Figure 6 | 4.3 | 1.4 | 1 | 9.8 | 6378 | 2885 |
| Figure 7 | 4.3 | 1.4 | 1 | 9.8 | 6378 | 2885 |
| Figure 8 | 4.3 | 1.4 | 1 | 9.8 | 6378 | 2885 |
| Figure 9 | 4.3 | 1.4 | 1 | 9.8 | 6378 | 2885 |
| Figure 10a | 4.3 | 1.4 | 0.7 | 9.8 | 6378 | 2885 |
| Figure 10b | 4.3 | 1.4 | 1 | 9.8 | 6378 | 2885 |
| Figure 10c | 4.3 | 1.4 | 1.5 | 9.8 | 6378 | 2885 |
| Figure 11 | 4.3 | 1.4 | 1.55–0.66 | 9.8 | 6378 | 2885 |
| Figure 12a | 4.3 | 1.4 | 0.7 | 8.9 | 6052 | 3000 |
| Figure 12b | 4.3 | 1.4 | 1 | 9.8 | 6378 | 2885 |
| Figure 12c | 4.3 | 1.4 | 1.5 | 3.7 | 3390 | 1800 |
| Figure 13a | 4.3 | 1.4 | 0.7 | 8.9 | 6052 | 3000 |
| Figure 13b | 4.3 | 1.4 | 1 | 9.8 | 6378 | 2885 |
| Figure 13c | 4.3 | 1.4 | 1.5 | 3.7 | 3390 | 1800 |
| Figure 14 | 1.4–14.3 | 1.4 | 0.89–0.63 | 9.8 | 6378 | 2885 |
| Figure 15 | 1.4–14.3 | 1.4 | 0.69 | 9.8 | 6378 | 2885 |
| Figure 16 | 1.4 | 1.4–14.3 | 1.55–0.63 | 9.8 | 6378 | 2885 |
| Figure 17 | 4.3 | 1.4 | 1.55–0.63 | 3.5–10.5 | 3000–7000 | 2885 |
| Figure 18 | 4.3 | 1.4 | 0–1.8 | 3.7; 9.8; 8.8 | 3390; 6378; 6052 | 1800; 2885; 3000 |

is outside the scope of this paper. Nevertheless, we calculate first-order estimates of the time required for complete solidification of the mantle and stop our calculation there.

[30] The presence of the massive greenhouse atmosphere results in a higher surface temperature and a slower cooling process. As seen in Figure 3e ($H_2O$, $CO_2$, and $N_2$ inventories of, respectively, 300, 100, and 5 bars), the surface temperature is much closer to the potential temperature in the presence of an atmosphere than when no atmosphere is present (Figure 3a). In addition, the greenhouse effect acts to increase the duration of the "Totally molten" and "Partially molten" stages, therefore delaying the mush stage (Figures 3b and 3f).

[31] At a threshold surface temperature above ≈2350 K, the upper layers of the atmosphere are hot, and the radiative temperature $T_{\mathrm{eff}}$ of the planet is in the range from 350 to 400 K [*Marcq*, 2012, Figure 1]. The net radiative flux from the atmosphere to space as given by $F_{\mathrm{atm}} = \sigma(T_{\mathrm{eff}}^4 - T_{\mathrm{eq}}^4)$ is high, the heat released by the magma ocean is radiated to space easily, and the atmosphere does not strongly counteract the radiative cooling of the planet. For the volatile content used in the calculation of *Marcq* [2012], the threshold temperature is around 2000 K. The time for a surface temperature of 2000 K to be reached is less than 1000 years without an atmosphere, and less than 100,000 years in the presence of an atmosphere, which remains short with respect to geological timescales (Figures 3a, 3b, 3i, and 3j). When the temperature drops below 2000 K, the high atmosphere rapidly cools and develops a substantial cloud cover. The radiative temperature is reduced to 230 K, thus slowing down the radiative cooling of the system. The duration of the partially molten stage increases from 1000 years when no atmosphere is present to more than 1 million years with an atmosphere (Figures 3a, 3b, 3i, and 3j).

[32] It is fortunate since very high atmospheric temperatures could cause thermal dissociation of the bulk atmospheric components ($CO_2$, $H_2O$) into lighter molecules (CO, $H_2$), thus altering the adiabatic lapse rate in the convective layer of the atmosphere, so that the thermal flux is underestimated through this process. However, if atmospheric quenching is strong enough, these lighter species could reach the radiative layers, and their extra opacity in the thermal infrared could diminish the thermal flux. Since these processes take place only at very high surface temperatures (over 2000 K), they can be safely ignored for the longest part of our simulations.

[33] When the overlying atmosphere is present, the magma ocean phase lasts 1.5 Myr, as opposed to 4 kyr when no atmosphere is present. These time estimates are in good agreement with the estimates of the duration of the magma ocean phase based on the scaling approach by *Solomatov* [2000, 2007], given that his estimate does not take into account the evolution of the heat flux with time. We also compared our results with those obtained with an atmosphere treated as a grey emitter (Figures 3e–3h) [*Elkins-Tanton*, 2008]. The duration of the partially molten stage, which is 200,000 years in the case where the atmosphere is treated as a grey emitter, is more than 1 million years according to our more realistic atmospheric model (note the "plateau" just before the mush stage on Figure 3h).

[34] Later, during the mush stage, the radiative cooling of the system slows down as well as the heat flux. Because we take into account the condensation of vapor water, we do not observe any decrease of the surface temperature during the mush stage for our model (Figure 3i). Indeed, the partial pressure of water vapor thus remains constant and stabilizes the surface temperature throughout this stage. Note that in Figure 3i, the surface temperature during the mush stage might be overestimated. Indeed, at that stage, atmospheric $CO_2$ heats the surface through greenhouse effect, and we do not consider in this paper the dissolution of $CO_2$ in the condensed water, a process that eventually resulted

in the formation of carbonates on Earth. If part of the $CO_2$ is sequestered in carbonates, the heating effect of $CO_2$ is reduced. This process could have played an important role in controlling the surface temperatures at the end of the solidification of the magma ocean.

### 3.2. Influence of $H_2O$ and $CO_2$ Volatiles

[35] Volatiles have a significant impact on the different characteristic times when they are exsolved and degassed to the atmosphere. Indeed, these gases promote greenhouse effect and influence the surface temperature significantly. If the total and final amount of volatile released in the atmosphere during solidification depends directly on the initial mass fractions of volatiles initially dissolved in the magma ocean, the way volatiles are released with time (degassing path) depends on the temporal evolution of the amount of magmatic liquid. Therefore, this evolution trend might be influenced either by the initial depth of the magma ocean or by the shape of the liquidus and solidus curves.

#### 3.2.1. Initial Mass Fractions of Volatiles

[36] Based on the knowledge of initial volatile content of protoplanets and accretion scenarios [e.g., *Raymond et al.*, 2006], it is likely that the initial water content at early times for terrestrial planets varies from almost 0 wt % to 5 wt %. The initial amount of volatiles dissolved in magma oceans is one of the key parameters governing the timing of solidification through greenhouse effect. In this section, we investigate the influence of the inventories of volatiles on the end of the magma ocean phase ($t_p$). The sensitivity study has been conducted for initial mass fractions of volatile species ($H_2O$ and $CO_2$) varying from $1.4\times10^{-2}$ wt % to $1.4\times10^{-1}$ wt %, that translate into global equivalent pressures varying from 100 to 1000 bars. Above a threshold of total gas pressure of 1000 bars, we attain the upper limit of the atmospheric model because the thickness of the atmosphere becomes too large regarding the other assumptions of the model.

[37] Figure 4 shows the evolution of the magma ocean phase duration ($t_p$) as a function of the initial $CO_2$ and $H_2O$ content. When varying one volatile component (from $1.4\times10^{-2}$ wt % to $1.4\times10^{-1}$ wt %), the other is kept at a constant initial amount of $1.4\times10^{-2}$ wt %. Time $t_p$ is quite sensitive to the initial $H_2O$ content, varying from 0.2 to almost 3 Myr, whereas for $CO_2$, the difference is only a few thousand years. This is because $H_2O$ has a greater radiative power than $CO_2$. Indeed, $H_2O$ absorbs infrared radiation over a wider range of wavelengths than $CO_2$. If we compare our results with the results obtained using a simpler treatment for the atmosphere such as a grey atmosphere (Figure 4), we find that the duration of the magma ocean phase is shorter of about an order of magnitude. This difference is probably due to an underestimation of the greenhouse effect in the latter case. If we now compare the duration of the magma ocean phase considering a grey atmosphere (150 kyr) with the results obtained by *Elkins-Tanton* [2008] for the same initial amount of volatile (60 kyr), we shed light on the effect of viscosity on the different time scales. Indeed, if we scale the energy conservation equation (2), we obtain an estimation of the convective cooling time scale [$t$], that is,

$$[t] \approx \frac{C_p \rho l T_p}{0.089k}\left(\frac{\alpha g}{\kappa \nu}\right)^{-1/3}[\Delta T]^{-4/3} \qquad (18)$$

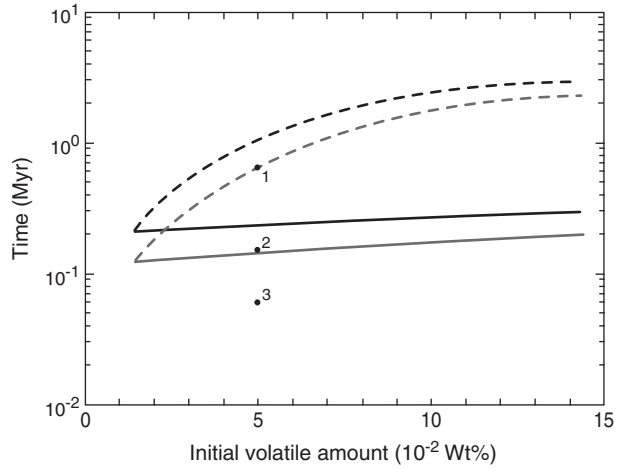


**Figure 4.** Duration of the magma ocean phase (black line) as a function of the initial mass fractions of $H_2O$ (dashed line) and $CO_2$ (solid line). For comparison, we also draw a dashed line corresponding to a threshold of 98% solidification in volume (grey line) [*Elkins-Tanton*, 2008]. Black dots correspond to the time required to solidify 98% of the magma ocean [*Elkins-Tanton*, 2008] when (1) coupling with our atmospheric model, (2) coupling with a grey atmosphere, and (3) using data from *Elkins-Tanton* [2008]. For these three cases, the initial content of $CO_2$ is $10^{-2}$ wt % and $H_2O$ $5\times10^{-2}$ wt %. Parameters used for these plots are given in Table 4.

with $\Delta T = T_p - T_s$ and other parameters defined in Table 1. If we consider equation (18) and given that viscosity is the only parameter that has different values for the two models when the atmosphere is treated as a grey emitter, the time scale ratio is proportional to the power 1/3 of the viscosity ratio. In our case, the magma viscosity reaches 4 Pa s in the last 20 kyr before $t_p$ which is 4–40 times more than the values used in *Elkins-Tanton* [2008]. The time difference between points 2 and 3 of Figure 4 is thus well explained by the viscosity difference between the two models. Figure 5 shows the degassing path for the two extreme cases of Figure 4, i.e., $1.4\times10^{-2}$ wt % $H_2O$ and $1.4\times10^{-1}$ wt % $H_2O$. It shows again that the difference in $t_p$ when the atmosphere is treated as a grey emitter and our more precise atmospheric model increases with the initial content of $H_2O$. These results seem to confirm an underestimation of the greenhouse effect in the case of the grey atmosphere. This plot also shows that $CO_2$ is exsolved at early times (99% is exsolved in a few hundred thousand years) because of its low solubility in magmas (equation (17)). Exsolution of water, on the contrary, occurs at the end of the partially molten stage when the melt becomes supersaturated in dissolved water. Figure 6 shows the solubility law for water in magmas, each dot representing the dissolved water content evolution with time. One can note that due to the specific shapes of the solidus and liquidus curves, the solidification process implies a rapid decrease in the liquid fraction and hence an increasing water mass fraction between 100 kyr and 1 Myr, corresponding to the observed peaks in volatile partial pressure in Figure 5. Note that in Figure 5, the final partial pressure $H_2O$ (condensed + uncondensed) does not

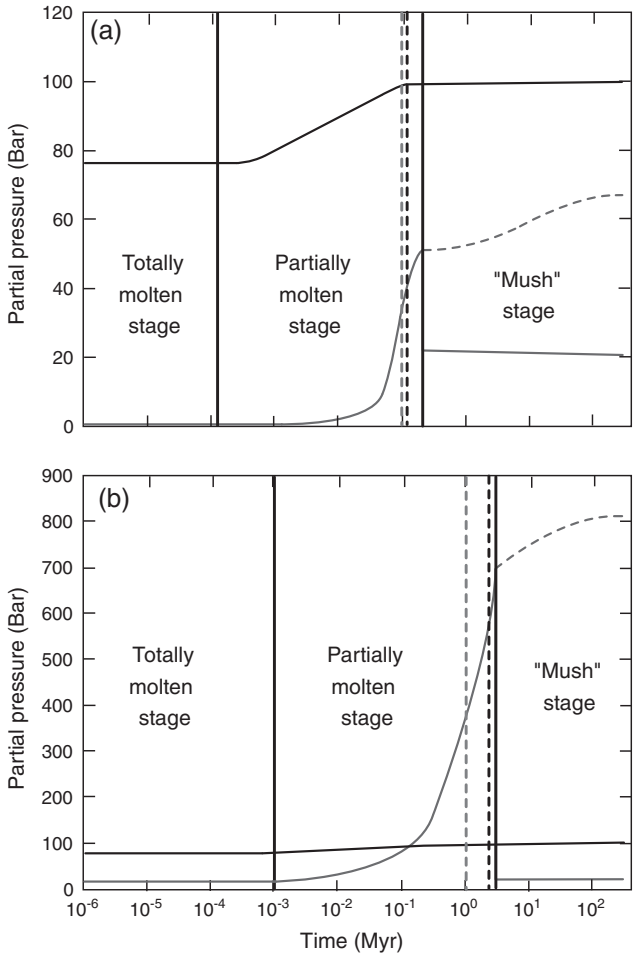


**Figure 5.** Time evolution of partial pressure of uncondensed $H_2O$ (grey line), total $H_2O$ (condensed and uncondensed) (grey dashed line) and $CO_2$ (black line) for an initial amount of $H_2O$ of (a) $1.4\times10^{-2}$ wt % and (b) $1.4\times10^{-1}$ wt %. The mass fraction of dissolved $CO_2$ is constant and equal to $1.4 \times 10^{-2}$ wt %. Condensation of water vapor occurs at the end of the magma ocean phase ($t_c = t_p$). It corresponds to the beginning of the mush stage shown by the vertical lines on the figure. For comparison, we also draw a dashed line corresponding to a threshold of 98% solidification in volume (grey line) [*Elkins-Tanton*, 2008]. Parameters used for the calculations are given in Table 4.

correspond to the initial amount dissolved in the magma ocean. This is due to the fact that some of the water is retained in the solid mantle.

### 3.2.2. The Liquidus-Solidus Curves

[38] The liquidus-solidus curves used in our model (Figure 1) are constructed from experimental data on lherzolite for a pressure less than 23 GPa [*Takahashi et al.*, 1993] and on perovskite for a pressure greater than 23 GPa [*Takahashi et al.*, 1993; *Zerr and Boehler*, 1993, 1994]. The irregularities in the curves observed at a depth of about 400 km correspond to a change in the mineralogy of the mantle between lherzolite and perovskite. Because the mineralogy of the early terrestrial planets might differ from a planet to another and also because the solidus and liquidus curves might present some uncertainties, we find interesting to study the influence of the shape of these solidus and liquidus profiles on the different characteristic times ($t_c$ time at which water vapor condenses and $t_p$). We compare the results obtained when using classical profiles of the liquidus-solidus as in *Abe* [1997] to simplified profiles approximated by straight lines.

[39] When the liquidus and solidus profiles are straight lines (Figure 7a), we observe that the volatile and especially water are exsolved later in the solidification history of the magma ocean (Figure 7c). We also observe that when using classical liquidus and solidus curves of Figure 7b, the mush stage and condensation of water vapor occur at a lower liquid fraction than in the case of using the straight curves of Figure 7a (see Figures 7b, 7c, 7e, and 7f).

[40] Figures 7b and 7e show the evolution of the liquid volume fraction of magma in the two considered cases. When we use "classical" solidus-liquidus curves, the volume of magma decreases more rapidly at the end of solidification due to the steep shape of the curve; as a result, there is a violent degassing of volatiles into the atmosphere at that time (Figure 7f). In the absence of such irregularities in the liquidus-solidus profiles (Figure 7a), there is a more gradual release of volatiles up to the end of the solidification of the magma ocean (Figure 7c). At the end of solidification, the total volatile content delivered into the atmosphere is the same for the two cases because we started with the same initial volatile content. One can note that the duration of the magma ocean phase is longer when the volume fraction of liquid is decreased in a short period of time than when the solidification is more gradual. It shows the close link between the solidification process and the evolution of the atmosphere composition due to degassing. Small variations in the shape of solidus and liquidus curves might have an important effect on the end of the magma ocean phase and on the time at which condensation of water occurs, in our case varying between 0.8 and 2 Myr.

### 3.2.3. The Initial Depth of the Magma Ocean

[41] Recent accretion models [e.g., *Raymond et al.*, 2006] show that there are still uncertainties concerning plausible scenarios for terrestrial planetary formation. Whether terrestrial planets underwent giant collisions during their

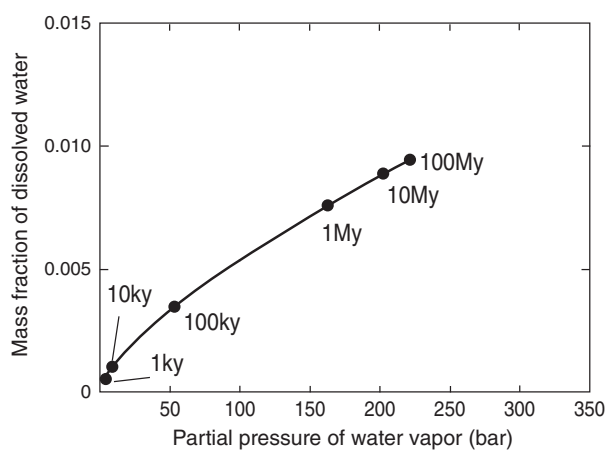


**Figure 6.** Mass fraction of water as a function of the partial pressure of water vapor after *Caroll and J. R. Holloway (Eds.)* [1994] (equation (16)). Parameters used for the calculations are given in Table 4.

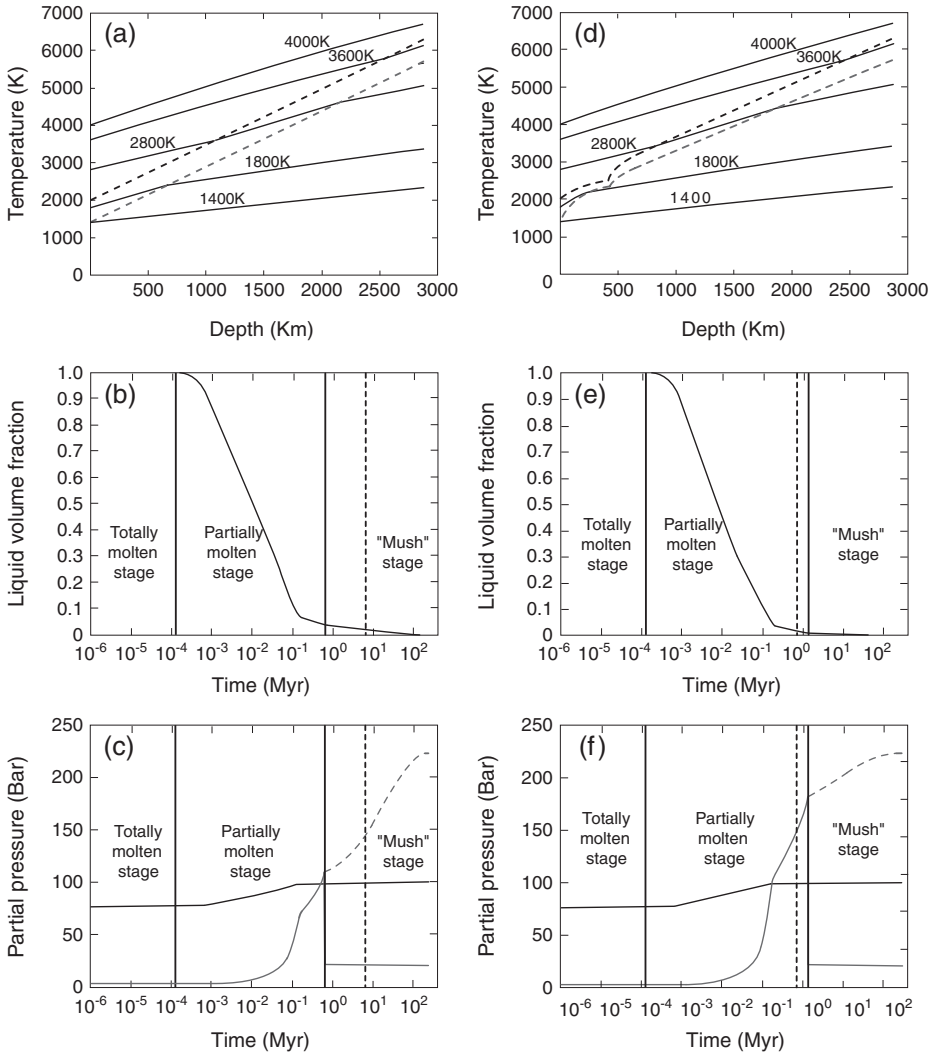


**Figure 7.** Evolution of (b–e) volumetric melt fraction, (c and f) partial pressure for (a and b) two different liquidus -solidus profiles defined in the main text. Condensation of water vapor occurs at the end of the magma ocean phase ($t_c = t_p$). It corresponds to the beginning of the mush stage shown by the vertical line on the figure. For comparison, we also draw a dashed line corresponding to a threshold of 98% solidification in volume (grey line) [*Elkins-Tanton*, 2008]. Parameters used for the calculations are given in Table 4.

formation is still a matter of debate [e.g., *Horner et al.*, 2009]. Given that the initial depth of the magma ocean depends on the speed and radius of the impactor and on the planet gravity, we want to investigate in this section different magma ocean depths possibly corresponding to different impact scenarios.

[42] It has been suggested that a giant impact with an impactor speed of about 10–15 km $s^{-1}$ is able to melt the entire planet and mantle [*Tonks and Melosh*, 1993]. If we consider the same initial amount of volatiles of $1.4\times10^{-2}$ wt % for $CO_2$ and $4.3\times10^{-2}$ wt % for $H_2O$, for a magma ocean depth of 500 km, $t_p$ is about 120 kyr, while for a completely molten mantle of 2885 km, $t_p$ is 1.4 Myr. This result was intuitively expected, as for the same initial mass fraction of volatiles, more $H_2O$ is released into the atmosphere for longer magma ocean depth.

### 3.3. Influence of the Radiogenic Heat Production Rate

[43] During planetary formation, internal heating is mainly produced by radiogenic elements contained in constitutive primitive material. Some radiogenic elements with a short period such as $^{26}Al$ produced abundant heat at the beginning of the solar system formation before rapidly disappearing and could be responsible for the differentiation of bodies which formed the planets [*Breuer and Moore*, 2007]. Other radiogenic elements such as U, Th, and K, which have a long period, have an influence at the end of the solidification of the magma ocean, when the heat flux becomes low. Long period elements do not impact the duration of the totally and partially molten stages, but increase the mush stage from 300 Myr to 1.5 Gyr (Figures 8a and 8b). In contrast, short period elements have an influence during the totally and partially molten stages (Figures 8b and 8c)

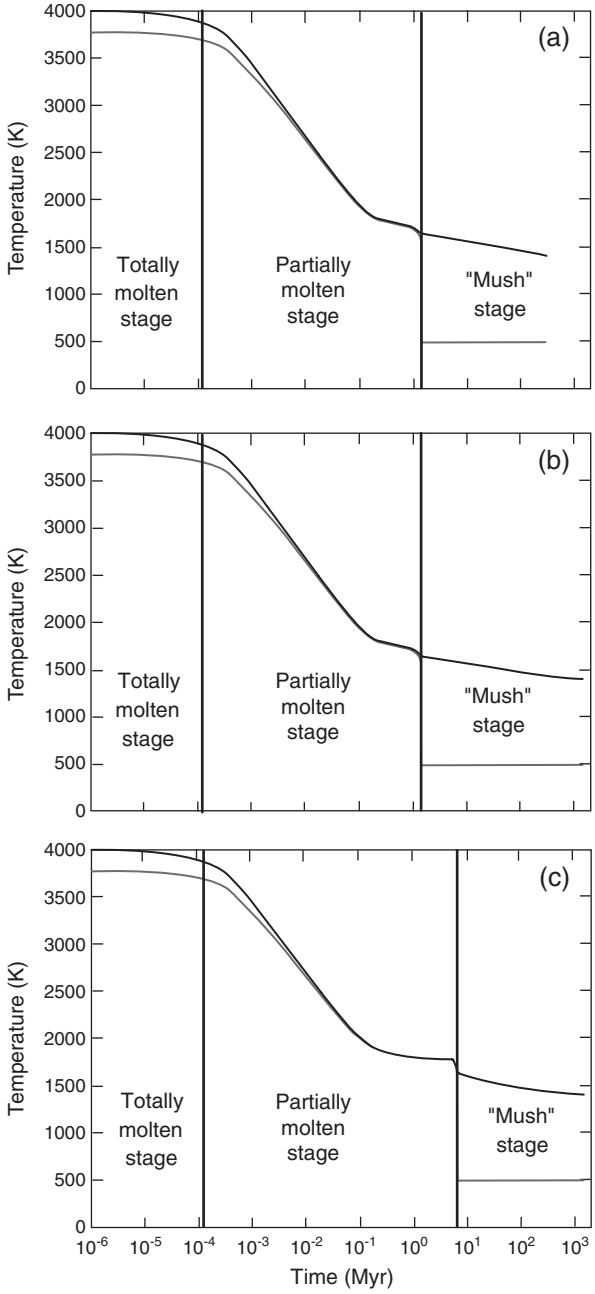


**Figure 8.** Time evolution of potential temperature (black line) and surface temperature (grey line) (a) without radiogenic heat production and with radiogenic heat produced by (b) U, Th, and K and by (c) U, Th, K, and $^{26}$Al. Condensation of water vapor occurs at the end of the magma ocean phase ($t_c = t_p$). It corresponds to the beginning of the mush stage shown by the vertical lines on the figure. For comparison, we also draw a dashed line corresponding to a threshold of 98% solidification in volume (grey line) [*Elkins-Tanton*, 2008]. Parameters used for the calculations are given in Table 4.

and increase the magma ocean phase duration ($t_p$) from 1 to 8 Myr. In Figure 8, the $^{26}$Al/$^{27}$Al ratio is chondritic, i.e., maximum; therefore, our estimation of $t_p \approx 8$ Myr is also maximum.

[44] Short period elements may have an influence only if terrestrial planets have been accreted very soon. The effect of the accretion duration on magma ocean duration through the energy released by radioactive decomposition of $^{26}$Al is shown in Figure 9. It may be seen that for an accretion period duration larger than 4.5 Myr, the effect of $^{26}$Al becomes negligible. Because terrestrial planets probably accreted definitively later than 10 Myr [*Raymond et al.*, 2006], short period radioactivity probably played a minor role.

### 3.4. Influence of the Distance From the Sun, Comparison Between Earth, Venus, and Mars

[45] In this section, we study the influence of the distance from the Sun on the duration of the magma ocean phase for totally molten planetary mantles. For that we first study the influence of solar flux alone by considering an Earth-like planet placed at the distances of Mars and Venus from the Sun. When Earth is placed at Venus' position, $t_p$ time is delayed significantly: approximately 1 Myr for the true Earth and 10 Myr when Earth is placed at the position of Venus (Figures 10a and 10b). On the contrary, at Mars' position, there is no influence of solar constant alone on the duration of the magma ocean phase (see Figure 10c).

[46] We then vary the position of the Earth in a range of distances corresponding to a solar flux in the range from 100 to 550 W m$^{-2}$, that is, from 1.55 to 0.66 AU (Figure 11) considering a solar constant of 957 W m$^{-2}$. Above a solar flux threshold of 540 W m$^{-2}$, corresponding to a distance from the Sun of 0.66 AU, the planet cannot release its excess heat to space, and the surface and potential temperatures are stabilized before reaching the mush stage.

[47] This threshold is related to the Nakajima limit [*Nakajima et al.*, 1992] and is different to that calculated by *Kasting* [1988]. Indeed, it appears that the main difference lies in the assumed planetary albedo: *Kasting* [1988] and *Abe and Matsui* [1988] derive an Earth-like albedo of 0.3, whereas Marcq assumes an albedo of 0.7 when thick clouds are found in the model (similar to present-day Venus). It may be therefore expected that the insolation limit will be higher

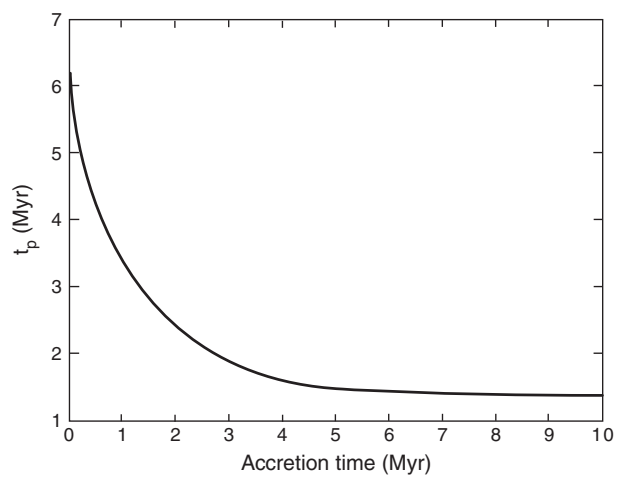


**Figure 9.** Magma ocean phase duration ($t_p$) as a function of the accretion time. Parameters used for the calculations are given in Table 4.

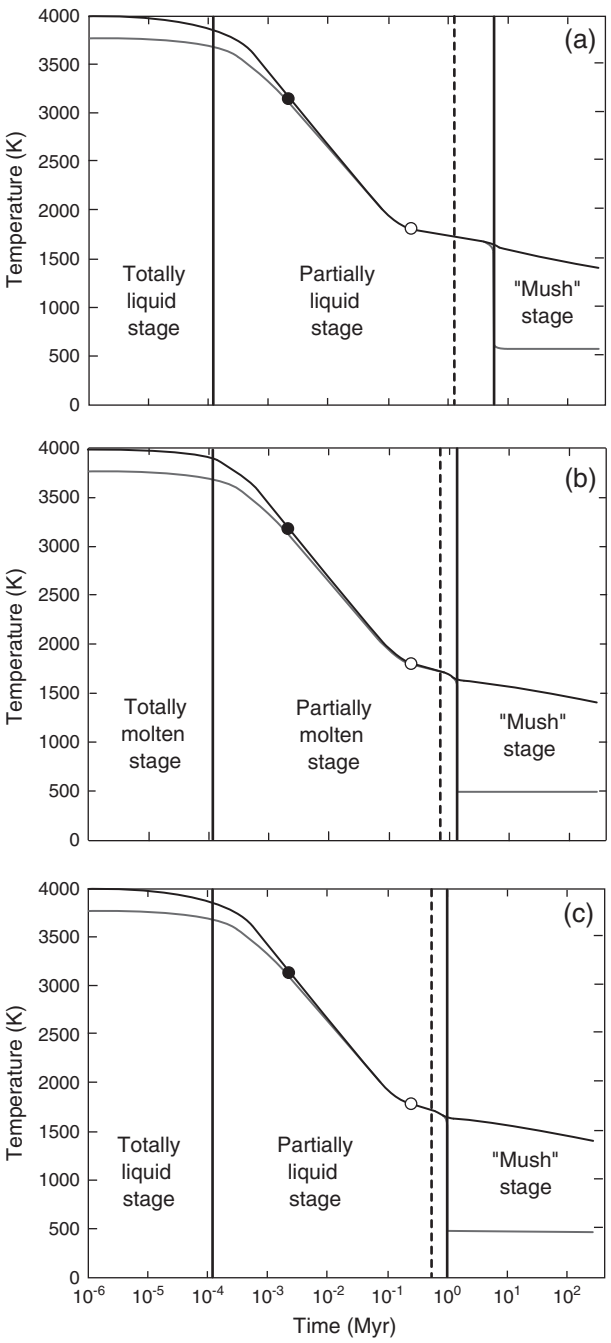


**Figure 10.** Time evolution of surface temperature (grey line) and potential temperatures (black line) of Earth for a distance from the Sun equal to that of (a) Venus, (b) the Earth, and (c) Mars. Condensation of water vapor occurs at the end of the magma ocean phase ($t_c = t_p$). It corresponds to the beginning of the mush stage and it is shown by the vertical lines on the figure. For comparison, we also draw a dashed line corresponding to a threshold of 98% solidification in volume (grey line) [*Elkins-Tanton*, 2008]. The black and white circles correspond to a solid state of 98% of the magma ocean [*Elkins-Tanton*, 2008] without atmosphere and with a grey atmosphere, respectively. Parameters used for the calculations are given in Table 4.

in such a case, since less solar light is absorbed. Actually, it is more meaningful to compare outgoing IR fluxes at this threshold (Nakajima limit) that should balance the absorbed solar radiation (at or near radiative equilibrium). *Kasting* [1988] and *Abe and Matsui* [1988] find a value close to 310 W m$^{-2}$ whereas *Marcq* [2012] finds a value close to 160 W m$^{-2}$. This discrepancy for Nakajima limit is discussed in *Marcq* [2012]: it appears that the 1980s era radiative model underestimated IR absorption because of the less sophisticated random band models required by the smaller available computing power. More recent, *k*-correlated computations of IR opacities yield thicker opacities and lower outgoing IR fluxes, as it is the case in *Marcq* [2012].

[48] Beyond this threshold, and provided that volatiles are not lost to space, the planet remains in the magma ocean phase. Venus, which is at 0.72 AU, is just outside this limit, below which magma ocean never freezes, but Mercury, which is at 0.4 AU from the Sun, is inside. Nevertheless, due to its small size, Mercury has been unable to prevent its atmosphere from escaping to space, and our model cannot be applied to Mercury.

[49] If we now consider the cooling history of a planetary mantle magma ocean for each telluric planet at its own position, we found that the duration of the magma ocean phase is not so different from the previous case for the Earth and Venus, which have similar radii (see Figures 10a, 10b, 12a, and 12b). Mars, however, remains in a totally molten stage longer than Earth because of its smaller radius (Figures 12b and 12c). Indeed, at the smaller pressure of the Martian mantle, the adiabats intersect the liquidus at lower temperatures values. In contrast, the time at which water vapor condenses is smaller than for the two other planets (see Figure 12c). Indeed, we considered accretion scenario for which initial mass fraction of volatiles is the same for the three planets; thus, for a smaller mantle depth, the amount of initial volatiles is smaller and the final atmosphere is more tenuous acting to reduce the greenhouse effect. We also draw on Figure 12 the time at which the mantle is solidified at 98%,

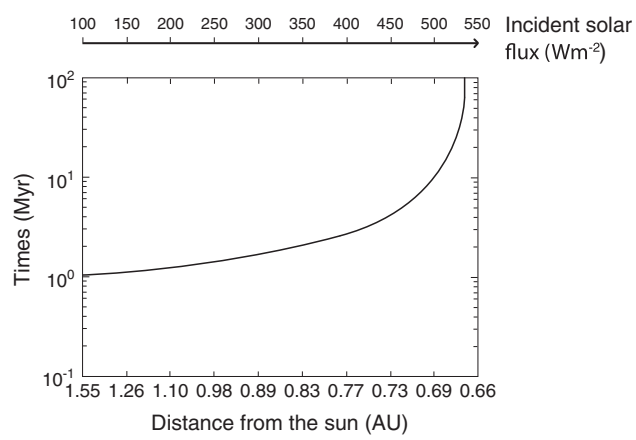


**Figure 11.** End of magma ocean phase as a function of the solar flux in a range of distances to the Sun from 1.55 AU (100 W m$^{-2}$) to 0.66 AU (550 W m$^{-2}$). Condensation of water vapor occurs at the end of the magma ocean phase ($t_c = t_p$). Parameters used for the calculations are given in Table 4.

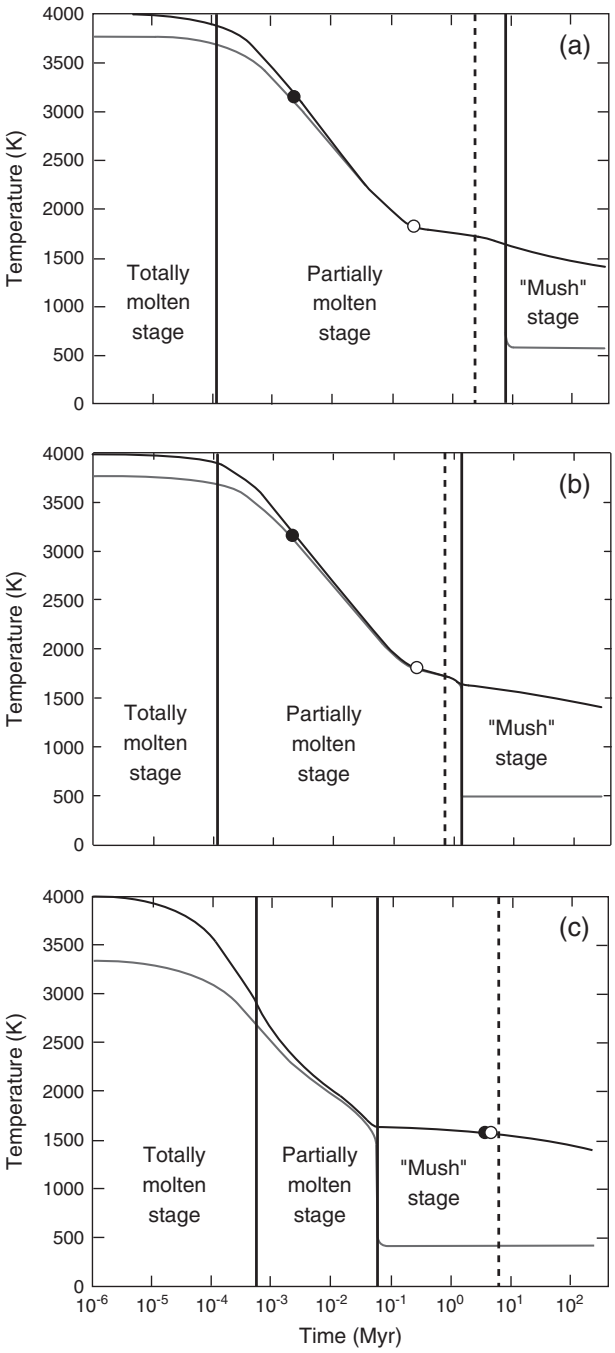


**Figure 12.** Time evolution of potential temperature (black line) and surface temperature (grey line) for (a) Venus, (b) the Earth, and (c) Mars. Condensation of water vapor occurs at the end of the magma ocean phase ($t_c = t_p$). It corresponds to the beginning of the mush stage shown by the vertical lines on the figure. For comparison, we also draw a dashed line corresponding to a threshold of 98% solidification in volume (grey line) [*Elkins-Tanton*, 2008]. The black and white circles represent times at which a solid state of 98% of the magma ocean is achieved when our model is not coupled with the atmosphere and when coupled with a grey atmosphere, respectively. Parameters used for the calculations are given in Table 4.

and we note that due to the relative shapes of temperature profiles and liquidus-solidus curves and the size of the mantle, the Martian mantle achieves later the same solidification stage than the two other planets. Figure 13 shows the partial pressures achieved in the atmosphere for the three planets. The duration of the magma ocean phase and condensation time is shorter from Mars to Venus: about 10 kyr for Mars, about 1 Myr for Earth, and 10 Myr for Venus.

## 4. Discussion

[50] The presence of the atmosphere acts to delay the formation of a cold and viscous surface boundary layer and increase the magma ocean phase duration. Once in the mush stage regime, the mantle viscosity increases, convection becomes less active, and the heat flux decreases. At this stage, the cooling time scale is controlled by the larger convection time scale, the atmosphere not being anymore a limiting factor for heat loss. On the contrary, when the magma ocean is totally or partially liquid, convection is active and the chemical composition of the atmosphere plays an important role through the greenhouse effect, thus controlling surface temperatures and cooling time scale. Indeed, without atmosphere, the surface temperature is on the order of 243 K (with an albedo of 0.2), a temperature corresponding approximately to the equilibrium temperature of the Earth. When an atmosphere composed of 300 bars $H_2O$ and 100 bars $CO_2$ overlays the magma ocean, the surface temperature reaches 490 K and remains constant throughout the mush stage (see Figure 3e). In our model, the water vapor exsolved from the magma ocean is instantaneously condensed, thus maintaining the atmospheric partial pressure of water vapor constant at a given surface temperature. As previously mentioned, the surface temperature is overestimated because we do not take into account the solubility of $CO_2$ into water nor the precipitation of carbonates.

[51] As shown in Figure 4 and due to its high radiative power, $H_2O$ content affects the magma ocean phase duration more than $CO_2$. If we now look at the effect of initial $H_2O$ content on the condensation time $t_c$, Figure 14 shows that for a solar flux below 450 W m$^{-2}$ (corresponding to a distance from the Sun of about 0.73 AU), the water is able to condense for all initial water contents. Above 450 W m$^{-2}$, condensation occurs only for water content higher than $1.8 \times 10^{-2}$ wt %. This counterintuitive trend is due to two competing effects: the greenhouse effect increasing surface temperature (favors the vapor phase) and a pressure effect increasing with the amount of water (favors the liquid phase; see Figure 15). In addition, at partial pressure of water vapor higher than approximately 50 bars, the surface temperature decreases with increasing pressure up to around 100 bars. This is due to the fact that at this threshold value, the infrared bands become saturated and the infrared flux becomes constant while the net solar flux continues to be decreased by Rayleigh scattering. Thus, the incoming solar radiation becomes insufficient to support the runaway greenhouse and water vapor can then condense [*Zahnle et al.*, 1988]. The arrow in Figure 15 shows the condensation path for an increasing initial water content for a solar flux of 500 W m$^{-2}$. An initial $CO_2$ content equivalent to a partial pressure of 500 bars is sufficient to prevent

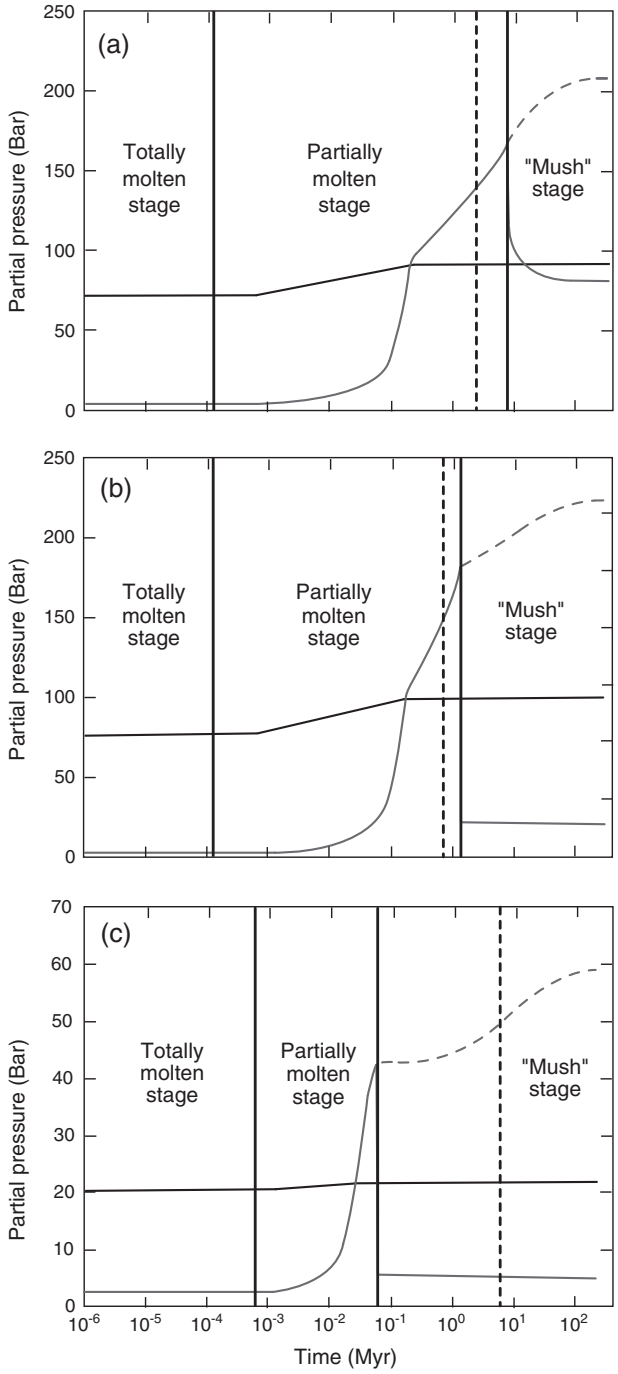


**Figure 13.** Time evolution of partial pressure of uncondensed $H_2O$ (grey line), total $H_2O$ (grey dashed line) and $CO_2$ (black line) for (a) Venus, (b) the Earth, and (c) Mars. Condensation of water vapor occurs at the end of the magma ocean phase ($t_c = t_p$). It corresponds to the beginning of the mush stage shown by the vertical lines on the figure. For comparison, we also draw a dashed line corresponding to a threshold of 98% solidification in volume (grey line) [*Elkins-Tanton*, 2008]. Parameters used for the calculations are given in Table 4.

condensation of water vapor on planets that would be located at a distance from the Sun closer than Mars (Figure 16). This result shows that for an atmospheric composition richer in water vapor than in $CO_2$, the effect of solar flux, and therefore distance from the Sun, has little effect on the condensation time for the planets that receive less than 450 W m$^{-2}$. However, for planets like Venus receiving a solar flux exceeding 450 W m$^{-2}$, condensation depends on their initial volatile composition.

[52] We then look at different planet sizes at different distances from the Sun (Figure 17). Below 400 W m$^{-2}$, condensation occurs regardless of the size of the planet. Above this value, for a given magma ocean depth (1500 km here) and a given volatile content, the smallest planets might never be able to sustain a water ocean. This is due to a lower value of atmospheric pressure (see Figure 15). Thus, a water ocean might never form on a planet located at the distance of Venus from the Sun if its radius is smaller than 4000 km. For example, a Mars-size planet located at the position of Venus might never have experienced the condensation of a water ocean throughout the magma ocean stage.

[53] Condensation of water vapor also depends on the albedo because it modifies the value of solar flux received at the surface of the planet. Thus, at a given distance from the Sun, a planet with a high albedo may condense water vapor while a planet with a smaller albedo may not (see Figure 18). The albedo depends on the the presence of clouds and may reach a value of about 0.7. As explained in section 3.4, our atmospheric model seems more accurate in calculations concerning albedo variations and computation of the IR absorption than the 1980s models [*Kasting*, 1988; *Abe and Matsui*, 1988].

[54] The time of appearance of a water ocean is 1 order of magnitude shorter for Mars, typically 0.1 Myr. Interestingly, this time is much shorter than the expected accretion time, typically 30 Myr [*Raymond et al.*, 2006]. A possible consequence could be the occurrence of serial water oceans growing on Earth and Mars, since the cooling time is definitely smaller than the time interval between major impacts (typically 5 million years for the few Mars-sized embryos which formed Earth). If so, atmospheric loss by impact could have been enhanced on these two planets during accretion due to the frequent presence of a layer of liquid water at the surface [*Genda and Abe*, 2005]. But the continuous accretion of small- and medium-sized embryos during the whole accretion period, enhancing the input energy flux above the level defined by solar flux alone, may result in a warmer surface and prevent atmospheric water vapor from condensing. From an isotopic analysis of SNC meteorites, *Debaille et al.* [2007] suggested that a magma ocean lasting at least 100 Myr had been present on Mars, which in first view does not agree with our results. Including the heating due to the primitive bombardment is the next step of the present work. The formation of continental crust 160 Myr after accretion of the Earth, which suggests that the Earth could have experienced a "cool early Earth" phase [*Valley et al.*, 2002], shows that liquid water was already present at the surface of Earth at this time. Our results reinforce the plausibility of such an early liquid water ocean, showing that it could have existed and stabilized as soon as just after the main accretion period, 100 Myr or less after the beginning of accretion.

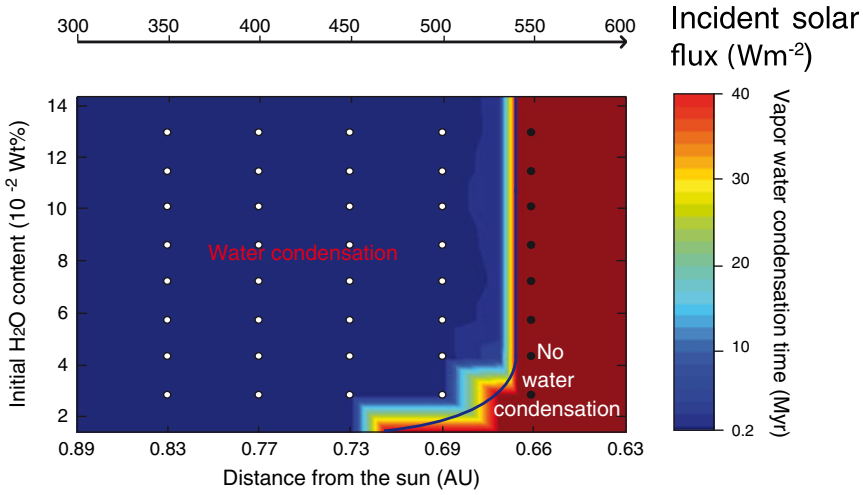


**Figure 14.** Diagram showing condition for condensation of water vapor as a function of initial $H_2O$ content and solar flux. Calculations are conducted for a planet with the physical characteristics of Earth. The initial amount of $CO_2$ is fixed at a value of $1.4 \times 10^{-2}$ wt % (corresponding to 100 bars). Color scale shows times at which condensation of water vapor occurs. Time increases from blue to red.

[55] Concerning Venus, our results suggest that the duration of the magma ocean phase is much larger than on the Earth, typically 10 Myr. This time is of the same order as the time interval between major impacts, and not much shorter than the whole accretion time (about 30 Myr from existing models). Consequently, Venus could have remained during several tens of millions of years, that is, the whole accretion duration, in the magma ocean stage due to the regular melting of its mantle by major impacts. Venus is just outside the distance of 0.66 AU from the Sun below which an Earth-type planet would remain in the magma ocean phase. According to our model, which does not take into account hydrodynamic escape at this stage, an Earth-type planet closer than 0.66 AU, and possibly Venus due to the regular occurrence of global melting events can remain in a stable, hot, configuration following $H_2O$ outgassing during a long time. Including H escape (and associated O frictional escape) would result in a progressive decrease of the $H_2O$ partial pressure [*Kasting and Pollack*, 1983; *Chassefière*, 1996, 1997; *Gillmann et al.*, 2009], therefore a weakening of the greenhouse effect and the condensation of the remaining water vapor at some later stage. Including hydrodynamic escape in our model is a necessary step for a more realistic simulation of magma ocean and water ocean formation and evolution.

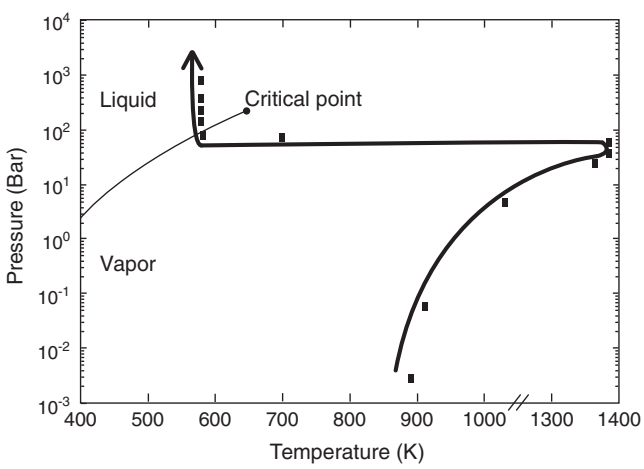


**Figure 15.** Phase diagram for $H_2O$. Condensation path for increasing water content (following the black arrow) from $4.3 \times 10^{-6}$ to $1.4 \times 10^{-1}$ wt %. The black squares represent several initial $H_2O$ amount with an initial $CO_2$ amount of $1.4 \times 10^{-2}$ wt % and a solar flux of 500 W $m^{-2}$. The partial pressure of water vapor and the surface temperature for each square are obtained at the end of the solidification of magma ocean ($T_p \approx 1400$ K).

[56] The occurrence, or non-occurrence, of a water ocean at the beginning of Venus' evolution, when the solar flux was definitely smaller than now, is a longstanding puzzling question. The critical point of $H_2O$ is located at 647 K. As shown by *Matsui and Abe* [1986], the surface temperature of Earth at the end of accretion could have been ≈600 K, therefore lower than the critical temperature, and water would have been able to condense, as confirmed by our results. From the same authors, the temperature of Venus surface at the end of the accretion was ≈700 K, larger than the critical temperature, potentially preventing atmospheric water from condensing out. *Kasting* [1988], taking into account the cooling effect of clouds (increasing the planetary albedo), suggested that a water ocean could have nevertheless formed at the beginning of Venus' evolution. Our results do not allow giving a definitive answer to this question. From the present model, a water ocean may possibly form on Venus typically 10 Myr after a major impact melting the mantle. About 10 major impacts occurring over a typical time of 30 Myr would be sufficient to prevent a water ocean from forming during accretion. But our results show that the formation of an ocean of water on Venus after accretion may or may not have happened, depending on both the initial amounts of volatiles ($H_2O$, $CO_2$) and any extra IR opacity

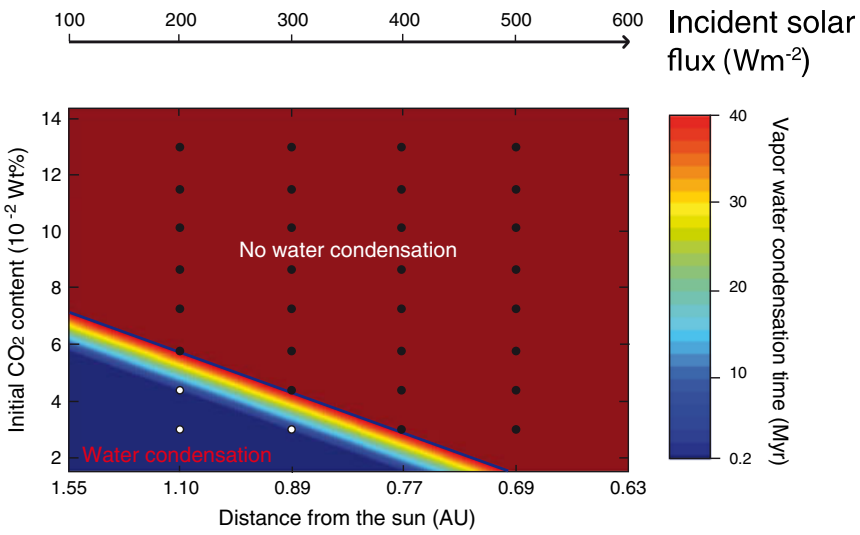


**Figure 16.** Diagram showing condition for condensation of water vapor as a function of initial $CO_2$ content and solar flux. Calculations are conducted for a planet with the physical characteristics of the Earth. The initial amount of water vapor is fixed at a value of $1.4 \times 10^{-2}$ wt % (corresponding to 100 bars). Color scale shows times at which condensation of vapor water occurs.

due to clouds or minor compounds. Our threshold for maintaining a greenhouse effect that keeps the surface of a planet similar to Earth molten in radiative equilibrium is 540 W $m^{-2}$ assuming an albedo of 0.7. This corresponds to a distance from the early Sun of 0.66 AU. Using the value of 480 W $m^{-2}$ derived by *Kasting* [1988] from models with not only a smaller IR opacity but also a smaller albedo of 0.36, this threshold distance would be 0.7 AU. If there are additional sources of opacity like sulfur and/or chlorine species, the IR opacity could be still increased, and the threshold distance be similar to, or larger than, Venus-Sun distance (0.71 AU), implying that water would never have condensed on Venus. Even by assuming that the IR opacity is correctly modeled, the initial volatile content is still able to prevent water from condensing: for $P_{(H_2O)} < 100$ bars (Figure 14) or $P_{(CO_2)} > 200$ bars (Figure 16), no condensation occurred in primitive Venus conditions. Such conditions are not unlikely. A major new result of the present work is that because the IR opacity modeled by using our *k*-correlated method is definitely larger than that modeled before and even assuming a large albedo, Venus is very close to the distance from the Sun below which water never condenses, making possible that no ocean ever formed.

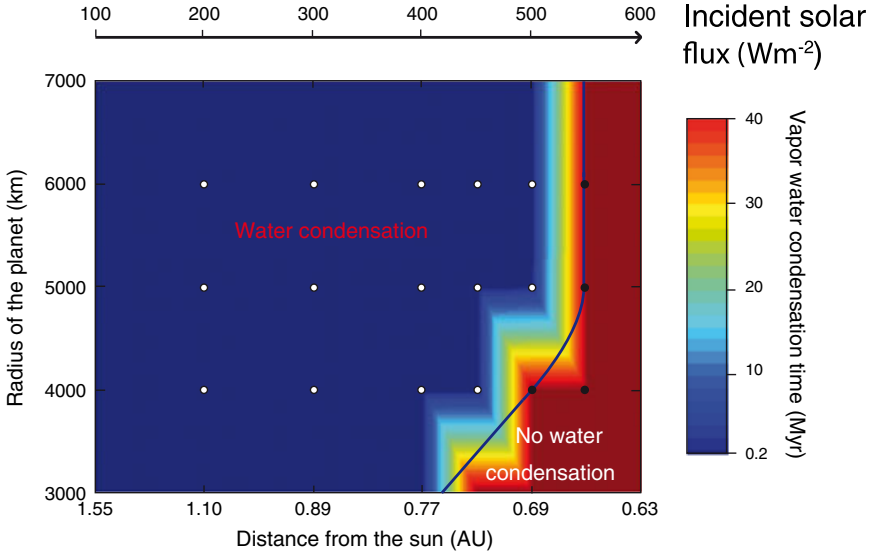


**Figure 17.** Diagram showing condition for condensation of water vapor as a function of radius of the planet and solar flux. Color scale shows times at which condensation of water vapor occurs. Time increases from blue to red.

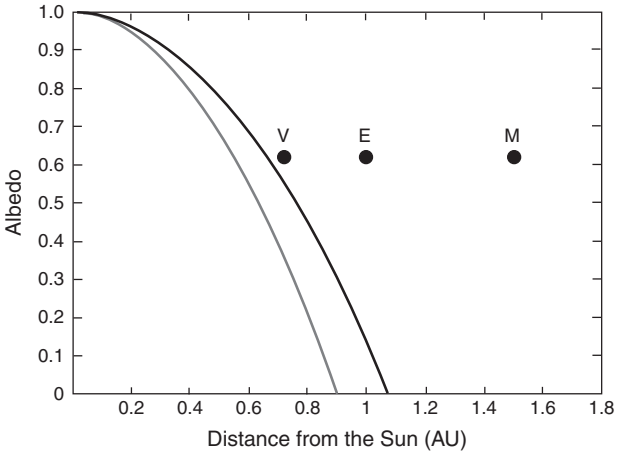


**Figure 18.** Water condensation limit (black line) as a function of the planet albedo and its distance from the sun. Note that the limit of condensation of water vapor obtained in our case is closer from Venus compared to previous work (grey line) [*Abe and Matsui*, 1988; *Kasting*, 1988]. Venus, Earth, and Mars are plotted for an albedo value of 0.63 corresponding to the mean albedo throughout solidification of the magma ocean.

## 5. Conclusion

[57] Our results suggest that after a major impact, the time for a planetary mantle magma ocean to cool and allow the condensation of the dense steam atmosphere into a water ocean is of the order of 1 Myr on Earth and depends on the various parameters mentioned in the previous sections. More generally,

[58] (i) The presence of the atmosphere delays the time at which a cold viscous thermal boundary layer forms by approximately 1 Myr compared to a case where no atmosphere is present.

[59] (ii) Volatiles' initial content, especially $H_2O$ and its degassing path, controls the duration of magma ocean phase increasing the duration of about 1 order of magnitude for 1 order of magnitude difference in initial content on Earth, with a few thousands years for $1.5 \times 10^{-2}$ wt % and 2 Myr for $1.5 \times 10^{-1}$ wt %. Deeper magma ocean or earlier degassing also increases magma ocean stage duration.

[60] (iii) Initial $CO_2$ content controls the ability to condense water ocean for distance from the Sun greater than 0.66 AU.

[61] (iv) For an accretion phase duration shorter than 5 Myr, the magma ocean phase duration might be twice longer when taking into account $^{26}$Al abundance at early times. The heat generated by long-lived elements such as U, Th, and K, is non-negligible only at the end of the solidification of the magma ocean when the heat flux falls below 10 W m$^{-2}$.

[62] This work has potentially important implications. First, it shows that Venus is close to the distance from the Sun (0.66 AU) below which an Earth-size planet remains in the magma ocean stage for a virtually infinite time. The typical time for an ocean of water on Venus to appear is of the order of 10 Myr, comparable to the duration of the main accretion sequence, suggesting that Venus could have remained in the magma ocean stage during most of its accretion. Our model shows that a water ocean may or may not have condensed on Venus after accretion, depending on the details of both IR radiative transfer and volatile inventory. A more realistic model including accretional heating due to small impacts and hydrodynamic escape is required for a more detailed analysis. Accretional heating and hydrodynamic escape of $H_2O$ are expected to play against the condensation of water, whereas hydrodynamic escape of $CO_2$ should favor the formation of an ocean. Second, the time for condensing a water ocean on Earth and Mars is smaller than 1 Myr (1 Myr for Earth and 0.1 Myr for Mars), suggesting that a water ocean could have formed in the periods between major impacts (able to melt a significant fraction of the mantle). If serial water oceans developed on Earth and Mars during their accretion, impact erosion of the atmosphere could have been more efficient on these planets, explaining their relatively tenuous atmosphere with respect to Venus. Concerning Mars, geochemical analyses of SNC meteorites suggest that the planet could have experienced a continuous magma ocean phase of ≈100 Myr [*Debaille et al.*, 2007], which contradicts the results of our model. The reason could be that we do not take into account the accretional heating resulting from the frequent impacts by small embryos.

[63] In this paper, we focused on the thermal evolution of one magma ocean cooling sequence. We do not consider the details of accretionary scenario. We assumed the presence of a magma ocean of a given depth (which depends on the energy injected in the system by a major impact) at a certain time of the accretion process, considered thereafter as the initial time in the model. Most of the results presented in this paper concern a completely molten magma ocean resulting from a giant impact [*Melosh*, 1990]. A realistic description of the full accretion sequence, with multiple impacts and serial magma ocean phases, was beyond the scope of the present paper. In particular, we do not take into account, at this stage, the energy released to the planet by the continuous flux of small impactors, adding to the input solar energy. The major goal of this paper was to conduct a parametric study in order to define which conditions may favor the formation of an early water ocean and the onset of plate growth, providing habitability criteria for a given planet under given conditions. Extending the accretion phase over a long period, and considering the effects of (i) major impacts melting large fractions of the mantle and (ii) frequent small impacts increasing the energy flux from the outside, (iii) realistic hydrodynamic escape model will be the subject of a second paper.

## Appendix A: Numerical Method

### A1. Time Loop

[64] From the solubility laws for $H_2O$ and $CO_2$ (equations (16) and (17)), we determine the partial pressure of each gas in the atmosphere. These partial pressures and the surface temperature allow to determine the heat flux at the top of the atmosphere. This heat flux must match the heat flux at the surface of the magma ocean. Therefore, an iterative loop is used to reach a balance between these fluxes. It is noted that the atmospheric model is limited by a threshold on the total pressure of gas of approximately

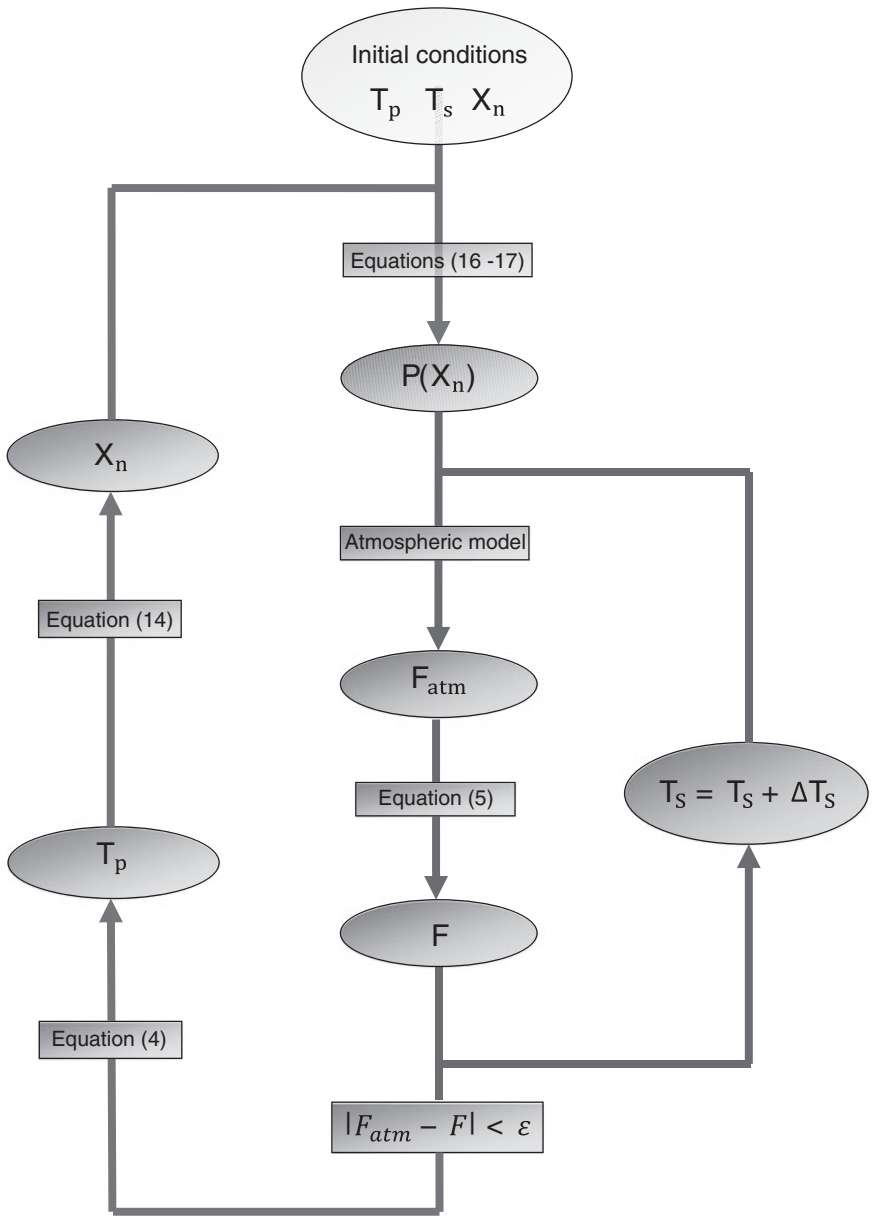


**Figure A1.** Flow chart of the numerical method.

1000 bars. Indeed, too much gas in the atmosphere would increase too much the thickness of the atmosphere and would skew the results obtained. Once the equality is satisfied, a new potential temperature is calculated at the next time step by using equation (4). New partial pressures are calculated, and the surface temperature calculated to the previous time step becomes the new initial surface temperature. The time step we take is adaptive. Indeed, we observed that the variation of the time step had little impact on the results. That is why, in order to limit the computation time, we adjusted the time step depending on the cooling rate determined by using equation (4).

### A2. Iterative Loop

[65] To balance the heat flux at the surface of the magma ocean and the atmospheric heat flux, we have implemented an iterative loop with a fixed stopping criterion for which $|F_{\mathrm{atm}} - F| < \epsilon$ where $\epsilon$ is equal to $10^{-1}$. This threshold is sufficient to consider that there is an equilibrium between these two fluxes. If this inequality is not satisfied, then the surface temperature is adjusted by a factor $\Delta T_s$ and the heat fluxes $F$ and $F_{\mathrm{atm}}$ are recalculated but with the same potential temperature and partial pressures of gas. Otherwise, the iterative loop terminates for this time step and we get a balanced heat flux between the two reservoirs and a surface temperature.

[66] A schematization of the numerical method is given in Figure A1.

## Appendix B: Temperature Profiles

[67] We suppose that the magma ocean is convecting vigorously so that the temperature distribution is quasi-adiabatic. For a one-phase system:

$$\frac{\mathrm{d}T}{\mathrm{d}P} = \frac{\alpha T}{\rho C_p}. \tag{B1}$$

[68] In the partially molten zone, the equation for an adiabat is given by [see *Solomatov*, 2007]

$$\frac{\mathrm{d}T}{\mathrm{d}P} = \frac{\alpha' T}{\rho C'_p}, \tag{B2}$$

with all variables being defined in the main text. Integrating equation (B1) between $R_l$ and $R_p$ in the liquid zone gives an expression for the temperature profile as a function of the potential temperature $T_p$:

$$T(r) = T_p \exp\left[\frac{\alpha g}{C_p}\left(R_p - r\right)\right], \tag{B3}$$

with $T(R_l) = T_p \exp\left[\frac{\alpha g}{C_p}\left(R_p - R_l\right)\right]$. In the partially molten zone, integrating equation (B2) gives

$$T(r) = T(R_l) \exp\left[\frac{\alpha' g}{C'_p}\left(R_l - r\right)\right], \tag{B4}$$

or expressed in terms of $T_p$,

$$T(r) = T_p \exp\left[\frac{\alpha g}{C_p}\left(R_p - R_l\right)\right] \exp\left[\frac{\alpha' g}{C'_p}\left(R_l - r\right)\right], \tag{B5}$$

[69] For convenience, we express all temperature profiles as a function of $R_p - r$, so that equation (B5) is rewritten as

$$T(r) = A\, T_p \exp\left[\frac{\alpha' g}{C'_p}\left(R_p - r\right)\right], \tag{B6}$$

with $A = \exp\left[\frac{\alpha g}{C_p}\left(R_p - R_l\right)\right] \exp\left[-\frac{\alpha' g}{C'_p}\left(R_p - R_l\right)\right]$. At the limit $R_s$ between the totally solid zone and partially molten zone, $T(R_s) = A\, T_p \exp\left[\frac{\alpha' g}{C'_p}\left(R_p - R_s\right)\right]$. In the solid zone, integrating equation (B1) gives

$$T(r) = T(R_s) \exp\left[\frac{\alpha g}{C_p}\left(R_s - r\right)\right], \tag{B7}$$

expressing equation (B8) as a function of $T_p$ and variable $R_p - r$ leads to

$$T(r) = A\, B\, T_p \exp\left[\frac{\alpha g}{C_p}\left(R_p - r\right)\right], \tag{B8}$$

with $B = \exp\left[-\frac{\alpha g}{C_p}\left(R_p - R_s\right)\right] \exp\left[\frac{\alpha' g}{C'_p}\left(R_p - R_s\right)\right]$.

[70] Given these temperature profiles, constant $I$ in equation (4) is written as

$$\begin{aligned} I = {} & \rho_m \left(C_p + \Delta H \frac{\mathrm{d}\phi}{\mathrm{d}T}\right) \int_{R_l}^{R_p} r^2 \exp\left(\frac{\alpha g (R_p - r)}{C_p}\right) \mathrm{d}r + \\ & A \int_{R_s}^{R_l} \rho \left(C'_p + \Delta H \frac{\mathrm{d}\phi}{\mathrm{d}T}\right) r^2 \exp\left(\frac{\alpha' g (R_p - r)}{C'_p}\right) \mathrm{d}r + \\ & B \rho_s \left(C_p + \Delta H \frac{\mathrm{d}\phi}{\mathrm{d}T}\right) \int_{R_b}^{R_s} r^2 \exp\left(\frac{\alpha g (R_p - r)}{C_p}\right) \mathrm{d}r \end{aligned} \tag{B9}$$

and

$$Q_r = \int_{R_b}^{R_p} r^2 \rho q_r \mathrm{d}r \tag{B10}$$

[71] Radii $R_l$, $R_s$, and $R_b$ are, respectively, the planetocentric altitudes of the bottom of the totally liquid zone, the top of the solid zone, and the bottom of the initially molten magma ocean (Figure 2), $g$ is the gravitational acceleration and $\alpha$ is the coefficient of volumetric thermal expansion.

[72] For a zone of partial melting, the coefficient of volumetric thermal expansion $\alpha'$ and the specific heat $C'_p$ are given as follows [*Solomatov*, 2007]:

$$\alpha' \sim \alpha + \frac{\Delta\rho}{\rho\left(T_{\mathrm{liq}} - T_{\mathrm{sol}}\right)} \tag{B11}$$

$$C'_p \sim C_p + \frac{\Delta H}{\left(T_{\mathrm{liq}} - T_{\mathrm{sol}}\right)} \tag{B12}$$

where $\Delta\rho$ is the density difference between solid and liquid. The thermal expansion coefficient is determined as follows [*Abe*, 1997]:

$$\alpha = \alpha_0 \left[\frac{PK'}{K_0} + 1\right]^{-(m-1+K')/K'} \tag{B13}$$

where $P$ is pressure in GPa, $\alpha_0 = 3 \times 10^{-5}$ K$^{-1}$, $K_0 = 200$ GPa, $K' = 4$, and $m = 0$ taken as the standard value.

[73] **Acknowledgments.** This work was supported by the French Space Agency CNES (Centre National d'Etudes Spatiales) and PNP (Programme National de Planétologie) from INSU (Institut National des Sciences de l'Univers). This work was funded by the interdisciplinary EPOV program of CNRS and ANR "PTECTO." We thank two anonymous reviewers for their careful and insightful reviews that greatly improve the manuscript.

## References

Abe, Y. (1993), Thermal evolution and chemical differentiation of the terrestrial magma ocean, *Geophys. Monogr.*, *74*, 41–54.

Abe, Y. (1995), Basic equations for evolution of partially molten mantle and core, in *The Earth's Central Part: Its Structure and Dynamics*, edited by T. Yukutake, pp. 215–235, TERRAPUB, Tokyo, Japan.

Abe, Y. (1997), Thermal and chemical evolution of the terrestrial magma ocean, *Phys. Earth Planet*, *100*, 27–39.

Abe, Y., and T. Matsui (1985), The formation of an impact-generated H20 atmosphere and its implications for the thermal history of the Earth, *J. Geophys. Res.*, *90*(suppl.), C545–C559.

Abe, Y., and T. Matsui (1986), Early evolution of the Earth: Accretion, atmosphere formation, and thermal history, *J. Geophys. Res.*, *91*(suppl.), E291–E302.

Abe, Y., and T. Matsui (1988), Evolution of an impact-generated $H_2O$-$CO_2$ atmosphere and formation of a hot proto-ocean on Earth, *J. Atmos. Sci.*, *45*, 3081–3101.

Ahlers, X. H., D. Funfschilling, H. Nobach, E. Bodenschatz, and G. Ahlers (2012), Transition to the ultimate state of turbulent Rayleigh-Bénard convection, *Phys. Rev. Lett.*, *108*, 024502.

Allègre, C. J., J.-P. Poirier, E. Humler, and A. W. Hofmann (1995), The chemical composition of the Earth, *Earth. Planet. Sci. Lett.*, *134*, 515–526.

Andrault, D., N. Bolfan-Casanova, G. L. Nigro, M. A. Bouhifd, G. Garbarino, and M. Mezouar (2011), Solidus and liquidus profiles of chondritic mantle: Implication for melting of the Earth across its history, *Earth. Planet. Sci. Lett.*, *304*, 251–259.

Androvandi, S., A. Davaille, A. Limare, A. Fouquier, and C. Marais (2011), At least three scales of convection in a mantle with strongly temperature-dependent viscosity, *Phys. Earth Planet. Int.*, *188*, 132–141.

Arzi, A. (1978), Critical phenomena in the rheology of partially melted rocks, *Tectonophysics*, *44*, 173–184.

Bercovici, D., Y. Ricard, and M. A. Richards (2000), The relation between mantle dynamics and plate tectonics: A primer, in *AGU Geophysical Monograph 21:* The History and Dynamics of Global Plate Motions, edited by M. A. Richards, R. Gordon, and R. Van der Hilst, AGU, Washington DC, 5–46.

Breuer, D., and W. B. Moore (2007), Dynamics and thermal history of the terrestrial planets, the Moon, and Io, *Treatise of Geophysics*, *7*, 89–165.

Caroll, M. R., and J. R. Holloway (Eds.) (1994), *Volatiles in Magma*, vol. 30, Mineralogical Society of America, Fredericksburg, Va.

Castaing, B., et al. (1989), Scaling of hard turbulence in Rayleigh-Bernard convection, *J. Fluid Mech.*, *204*, 1–30.

Chassefière, E. (1996), Hydrodynamic escape of hydrogen from a hot water-rich atmosphere: The case of Venus, *J. Geophys. Res.*, *101*, 26,039–26,056.

Chassefière, E. (1997), Loss of water on the young Venus: The effect of a strong primitive solar wind, *Icarus*, *126*, 229–232.

Chavanne, X., F. Chilà, B. Castaing, B. Hébral, B. Chabaud, and J. Chaussy (1997), Observation of the ultimate regime in Rayleigh-Bénard convection, *Phys. Rev. Lett.*, *79*(19), 3648–3651.

Conrad, C. P., and B. H. Hager (1999), Effects of plate bending and fault strength at subduction zones on plate dynamics, *J. Geophys. Res.*, *104*, 17,551–17,571, doi:10.1029/1999JB900149.

Davaille, A., and A. Limare (2007), Laboratory studies of mantle convection, *Treatise of Geophysics*, *7*, 89–165.

Davies, G. F. (1999), *Dynamic Earth: Plates, Plumes, and Mantle Convection*, 458, Cambridge University Press, Cambridge, UK.

Debaille, V., A. D. Brandon, Q. Y. Yin, and B. Jacobsen (2007), Coupled 142nd-143nd evidence for a protoacted magma ocean in Mars, *Nature*, *450*, 525–528.

Elkins-Tanton, L. (2008), Linked magma ocean solidification and atmospheric growth for Earth and Mars, *Earth. Planet. Sci. Lett.*, *271*, 181–191.

Elkins-Tanton, L. (2012), Magma oceans in the inner solar system, *Annu. Rev. Earth Planet. Sci.*, *40*, 113–139.

Fiquet, G., A. L. Auzende, J. Siebert, A. Corgne, H. Bureau, H. Ozawa, and G. Garbarino (2010), Melting of peridotite to 140 gigapascals, *Science*, *329*, 1516–1518.

Genda, H., and Y. Abe (2005), Enhanced atmospheric loss on protoplanets at the giant impact phase in the presence of oceans, *Nature*, *433*, 842–844.

Gillmann, C., E. Chassefière, and P. Lognonné (2009), A consistent picture of early hydrodynamic escape of Venus atmosphere explaining present Ne and Ar isotopic ratios and low oxygen atmospheric content, *Earth Planet. Sci. Lett.*, *286*, 503–513.

Grossmann, S., and D. Lohse (2000), Scaling in thermal convection: A unifying theory, *J. Fluid Mech.*, *407*, 27–56.

Hirschmann, M. M. (2009), Partial melt in the oceanic low velocity zone, *Phys. Earth Planet. Inter.*, *179*, 60–71.

Horner, J., O. Mousis, J.-M. Petit, and B. W. Jones (2009), Differences between the impact regimes of the terrestrial planets: Implications for primordial d:h ratios, *Planet. Space Sci.*, *57*, 1338–1345.

Hostetler, C. J., and M. J. Drake (1980), On the early global melting of the terrestrial planets, *Proceeding of the 11th Lunar and Planetary Science Conference,* pp. 1915–1929, Houston, Tex.

Jaupart, C., and G. Brandeis (1986), The stagnant bottom layer of convecting magma chambers, *Earth. Planet. Sci. Lett.*, *80*, 183–199.

Jaupart, C., and J.-C. Mareschal (2011), *Heat Generation and Transport in the Earth*, Cambridge University Press, New York.

Javoy, M. (1999), Chemical earth models, *C. R. Acad. Sci. Paris*, *329*, 537–555.

Karato, S. I., and P. Wu (1993), Rheology of the upper mantle: A synthesis, *Science*, *260*, 771–778.

Karki, B. B., and L. P. Stixrude (2010), Viscosity of $MgSiO_3$ liquid at Earth's mantle conditions: Implications for an early magma ocean, *Science*, *328*, 740–742.

Kasting, J. F. (1988), Runaway and most greenhouse atmospheres and the evolution of Earth and Venus, *Icarus*, *74*, 472–494.

Kasting, J. F., and J. B. Pollack (1983), Loss of water from Venus. I. Hydrodynamic escape of hydrogen, *Icarus*, *53*, 479–508.

King, E. M., S. Stellmach, and J. M. Aurnou (2012), Heat transfer by rapidly rotating Rayleigh-Bénard convection, *J. Fluid Mech.*, *691*, 568–582.

Korenaga, J. (2006), Archean geodynamics and the thermal evolution of Earth, in Archean Geodynamics and Environments: Geophysical Monograph, *64*, edited by K. Benn et al., pp. 7–32, AGU, Washington, D. C.

Kraichman, R. H. (1962), Turbulent thermal convection at arbitrary Prandtl number, *Phys. Fluid.*, *5*, 1374–1389.

Labrosse, S., J. W. Hernlund, and N. Coltice (2007), A crystallizing dense magma ocean at the base of Earth's mantle, *Nature*, *450*, 866–869.

Lodders, K., and B Fegley (1998), *The Planetary Scientist's Companion*, Oxford University Press, New York.

Lowman, J. P. (2011), Mantle convection models featuring plate tectonic behavior: An overview of methods and progress, *Tectonophysics*, *510*, 1–16.

Malkus, W. V. R. (1954), Discrete transitions in turbulent convection, *Proc. R. Soc. Lond. A*, *225*, 185–195.

Marcq, E. (2012), A simple 1d radiative-convective atmospheric model designed for integration into coupled models of magma ocean planets, *J. Geophys. Res*, *117*, E01,001.

Matsui, T., and Y. Abe (1986), Evolution of an impact-induced atmosphere and magma ocean on the accreting Earth, *Nature*, *319*, 303–305.

McDonougha, W. F., and S.-s. Sun (1995), The composition of the Earth, *Chem. Geol.*, *120*, 223–253.

Mei, S., W. Bai, T. Hiraga, and D. L. Kohlstedt (2002), Influence of melt on the creep behavior of olivine-basalt aggregates under hydrous conditions, *Earth Planet. Sci. Lett.*, *201*, 491–507.

Melosh, H. J. (1990), Giant impacts and the thermal state on the early Earth, in *Origin of the Earth*, edited by H. Newsom, and J. Jones, pp. 69–83, Oxford University Press, New York.

Nakajima, S., Y. Hayashi, and Y. Abe (1992), A study on the "runaway greenhouse effect" with a one-dimensional radiative-convective equilibrium model, *J. Atmos. Sci.*, *49*, 2256–2265.

Nomura, R., H. Ozawa, S. Tateno, K. Hirose, J. Hernlund, S. Muto, H. Ishii, and N. Hiraoka (2011), Spin crossover and iron-rich silicate melt in the Earth's deep mantle, *Nature*, *473*, 199–202.

Pan, V., J. R. Holloway, and R. L. Hervig (1991), The pressure and temperature dependence of carbon dioxide solubility in tholeiitic basalt melts, *Geochim. Cosmochim. Acta.*, *55*, 1587–1595.

Priestley, C. H. B. (1957), Convection from the Earth's surface, *Proc. R. Soc. Lond.*, *A238*, 287–304.

Priestley, C. H. B. (1959), *Turbulent Transfer in Lower Atmosphere*, 130, Univ. Chicago Press, Chicago.

Rasool, S. I., and C. de Bergh (1970), The runaway greenhouse and accumulation of $CO_2$ in the Venus atmosphere, *Nature*, *226*, 1037–1039.

Raymond, S. N., T. Quinn, and J. I. Lunine (2006), High-resolution simulations of the final assembly of earth-like planets. I. Terrestrial accretion and dynamics, *Icarus*, *183*, 265–282.

Reese, C., and V. S. Solomatov (2006), Fluid dynamics of local martian magma oceans, *Icarus*, *184*, 102–120.

Roscoe, R (1952), The viscosity of suspensions of rigid spheres, *Br. J. Appl. Phys.*, *3*, 267–269.

Rybach, L (1988), Determination of heat production rate, in *Handbook of Terrestrial Heat-Flow Density Determination*, edited by R. Haenel et al., pp. 125–142, Kluwer Academic Publishers, The Netherlands.

Samuel, H. (2012), A re-evaluation of metal diaper breakup and equilibration in terrestrial magma oceans, *Earth. Planet. Sci. Lett.*, *313-314*, 105–114.

Schubert, G., D. L. Turcotte, and P. Olson (2001), *Mantle in the Earth and Planets*, Cambridge University Press, Cambridge, U. K.

Shimazu, Y., and T. Urabe (1968), An energetic study of the evolution of the terrestrial and cytherean atmospheres, *Icarus*, *9*, 498–506.

Siggia, E. D. (1994), High Rayleigh number convection, *Annu. Rev. Fluid Mech.*, *26*, 137–168.

Solomatov, V. S., and L. N. Moresi (1997), Three regimes of mantle convection with non-Newtonian viscosity and stagnant lid convection on the terrestrial planets, *Geophys. Res. Lett.*, *24*, 1907–1910.

Solomatov, V. (2000), Fluid dynamics of magma oceans, in *Origin of the Earth and Moon*, edited by R. Canup, and K. Righter, pp. 323–338, Univ. of Arizona Press, Tucson, Ariz.

Solomatov, V. S. (2007), Magma oceans and primordial mantle differentiation, *Treatise on Geophysics*, *9*, 91–120.

Sramek, O., L. Milelli, Y. Ricard, and S. Labrosse (2011), Thermal evolution and differentiation of planetesimals and planetary embryos, *Icarus*, *217*, 339–354.

Suckale, J., J. A. Sethian, J. Yu, and L. T. Elkins-Tanton (2012), Crystals stirred up: 1. Direct numerical simulations of crystal settling in nondilute magmatic suspensions, *J. Geophys. Res.*, *117*, E08004.

Takahashi, E., T. Shimazaki, Y. Tsuzaki, and H. Yoshida (1993), Melting study of a peridotite klb-1 to 6.5 gpa, and the origin of basaltic magmas, *Phil. Trans. R. Soc. Lond. A*, *342*, 105–120.

Taylor, S. R., and S. M. McLennan (1995), The geochemical evolution of the continental crust, *Reviews of Geophysics*, *33*, 241–265.

Tonks, W. B., and H. J. Melosh (1993), Magma ocean formation due to giant impacts, *J. Geophys. Res.*, *98*, 5319–5333.

Turner, J. S., and I. H. Campbell (1986), Convection and mixing in magma chambers, *Earth-Sciences Reviews*, *23*, 255–352.

Valley, J. W., W. H. Peck, E. M. King, and S. A. Wilde (2002), A cool early earth, *Geology*, *30*, 351–354.

Van Hunen, J., P. E. van keken, A. Hynes, and G. F. Davies (2008), *Tectonics of Early Earth: Some Geodynamic Considerations,* edited by

K. C. Condie and V. Pease, p. 440, The Geological Society of America Special Paper, Boulder, Colo.

Wood, J. A., J. S. Dickey, U. B. Marvin, and B. N. Powell (1970), Anorthosites and a geophysical model of the moon, *Proceedings of the Apollo 11 Lunar Planetery Science Conference,* pp. 965–988, Houston, Tex.

Zahnle, K. J., J. F. Kasting, and J. B. Pollack (1988), Evolution of a steam atmosphere during Earth's accretion, *Icarus*, *74*, 62–97.

Zahnle, K., N. Arndt, C. Cockell, A. Halliday, E. Nisbet, F. Selsis, and N. H. Sleep (2007), Emergence of a habitable planet, *Space Sci. Rev.*, *129*, 35–78.

Zerr, A., and R. Boehler (1993), Melting of (Mg, Fe) $SiO_3$-perovskite to 625 kilobars: Indication of a high melting temperature in the lower mantle, *Science*, *262*, 553–555.

Zerr, A., and R. Boehler (1994), Constraints on the melting temperature of the lower mantle from high-pressure experiments on mgo and magnesiowustite, *Nature*, *371*, 506–508.